nature cell biology

ARTICLES

https://doi.org/10.1038/s41556-021-00705-x

Check for updates

Niche stiffening compromises hair follicle stem cell potential during ageing by reducing bivalent promoter accessibility

Janis Koester[1,2], Yekaterina A. Miroshnikova[1,2,3,4,5], Sushmita Ghatak[1], Carlos Andrés Chacón-Martínez[1], Jessica Morgner[1], Xinping Li[1], Ilian Atanassov[1], Janine Altmüller[6], David E. Birk[7], Manuel Koch[8,9], Wilhelm Bloch[10], Michaela Bartusel[9], Carien M. Niessen[2,9,11], Alvaro Rada-Iglesias[2,9,12] and Sara A. Wickström[1,2,3,4,5] ✉

Tissue turnover requires activation and lineage commitment of tissue-resident stem cells (SCs). These processes are impacted by ageing, but the mechanisms remain unclear. Here, we addressed the mechanisms of ageing in murine hair follicle SCs (HFSCs) and observed a widespread reduction in chromatin accessibility in aged HFSCs, particularly at key self-renewal and differentiation genes, characterized by bivalent promoters occupied by active and repressive chromatin marks. Consistent with this, aged HFSCs showed reduced ability to activate bivalent genes for efficient self-renewal and differentiation. These defects were niche dependent as the transplantation of aged HFSCs into young recipients or synthetic niches restored SC functions. Mechanistically, the aged HFSC niche displayed widespread alterations in extracellular matrix composition and mechanics, resulting in mechanical stress and concomitant transcriptional repression to silence promoters. As a consequence, increasing basement membrane stiffness recapitulated age-related SC changes. These data identify niche mechanics as a central regulator of chromatin state, which, when altered, leads to age-dependent SC exhaustion.

All multicellular organisms undergo a decline in tissue and organ function as they age. Loss in SC number and/or activity over time has been proposed to be responsible for this decline[1]. Consistent with the SC ageing hypothesis, SC ageing phenotypes have been described for multiple tissues, including the haematopoietic system, intestine, muscle, brain, skin and germline[2]. However, how ageing mechanistically impacts adult SC function and tissue maintenance is not fully clear.

SCs must safeguard their undifferentiated state while ensuring stringent governance of differentiation trajectories. Mammalian SCs, in particular embryonic SCs, display a unique epigenetic and transcriptional state, termed the poised or bivalent state, characterized by the simultaneous promoter occupancy of histone methylation marks indicative of both active and silenced states, trimethylation of lysine 4 of histone 3 (H3K4me3) and trimethylation of lysine 27 of histone 3 (H3K27me3), respectively[3]. The function of this bivalent state is to enable these genomic loci to rapidly respond to developmental cues while at the same time being refractory to subthreshold noise[3,4].

The adult quiescent hair follicle stem cells (HFSCs) drive regeneration of hair through cyclical bouts of rest (telogen), growth (anagen) and regression (catagen). At the start of each cycle, HFSCs residing in the bulge niche are activated to proliferate and subsequently differentiate to supply the cells needed for hair follicle down-growth. During catagen, the non-permanent part of the hair follicle regresses and the HFSCs resume quiescence until the next hair cycle[5]. These well-understood dynamics make HFSCs an ideal system to study age-related defects in SC regulation and tissue maintenance.

In this Article, we investigate the fundamental mechanisms of SC ageing by determining age-dependent alterations in the chromatin landscape of murine HFSCs and addressing the causes and functional implications of these chromatin changes. Our results identify a key role for the mechanical state of the aged HFSC niche impacting chromatin accessibility, and the epigenetic state of key activation, self-renewal and differentiation genes. This niche-dependent reduction in promoter accessibility results in attenuated SC activation and tissue regeneration. Thus, this study implicates tissue stiffening as a key regulator of SC potential in ageing.

Results

HFSC ageing leads to reduced chromatin accessibility. Skin ageing is associated with a reduced potency of HFSCs, already at stages during which HFSCs are still present at numbers comparable to young mice[6–8]. Later during ageing, severe hair loss has been reported, which is associated with hair follicle destruction and reduced HFSC

[1]Max Planck Institute for Biology of Ageing, Cologne, Germany. [2]Cologne Excellence Cluster for Stress Responses in Ageing-associated diseases (CECAD), University of Cologne, Cologne, Germany. [3]Helsinki Institute of Life Science, Biomedicum Helsinki, University of Helsinki, Helsinki, Finland. [4]Wihuri Research Institute, Biomedicum Helsinki, University of Helsinki, Helsinki, Finland. [5]Stem Cells and Metabolism Research Program, Faculty of Medicine, University of Helsinki, Helsinki, Finland. [6]Cologne Center for Genomics, University of Cologne, Cologne, Germany. [7]Department of Molecular Pharmacology & Physiology, University of South Florida, Morsani College of Medicine, Tampa, FL, USA. [8]Institute for Dental Research and Oral Musculoskeletal Research, Center for Biochemistry, University of Cologne, Cologne, Germany. [9]Center for Molecular Medicine Cologne (CMMC), University of Cologne, Cologne, Germany. [10]Molecular and Cellular Sport Medicine, German Sport University Cologne, Cologne, Germany. [11]Department of Dermatology, Center for Molecular Medicine, University of Cologne, Cologne, Germany. [12]Institute of Biomedicine and Biotechnology of Cantabria (IBBTEC), University of Cantabria/CSIC, Cantabria, Spain. ✉e-mail: sara.wickstrom@helsinki.fi

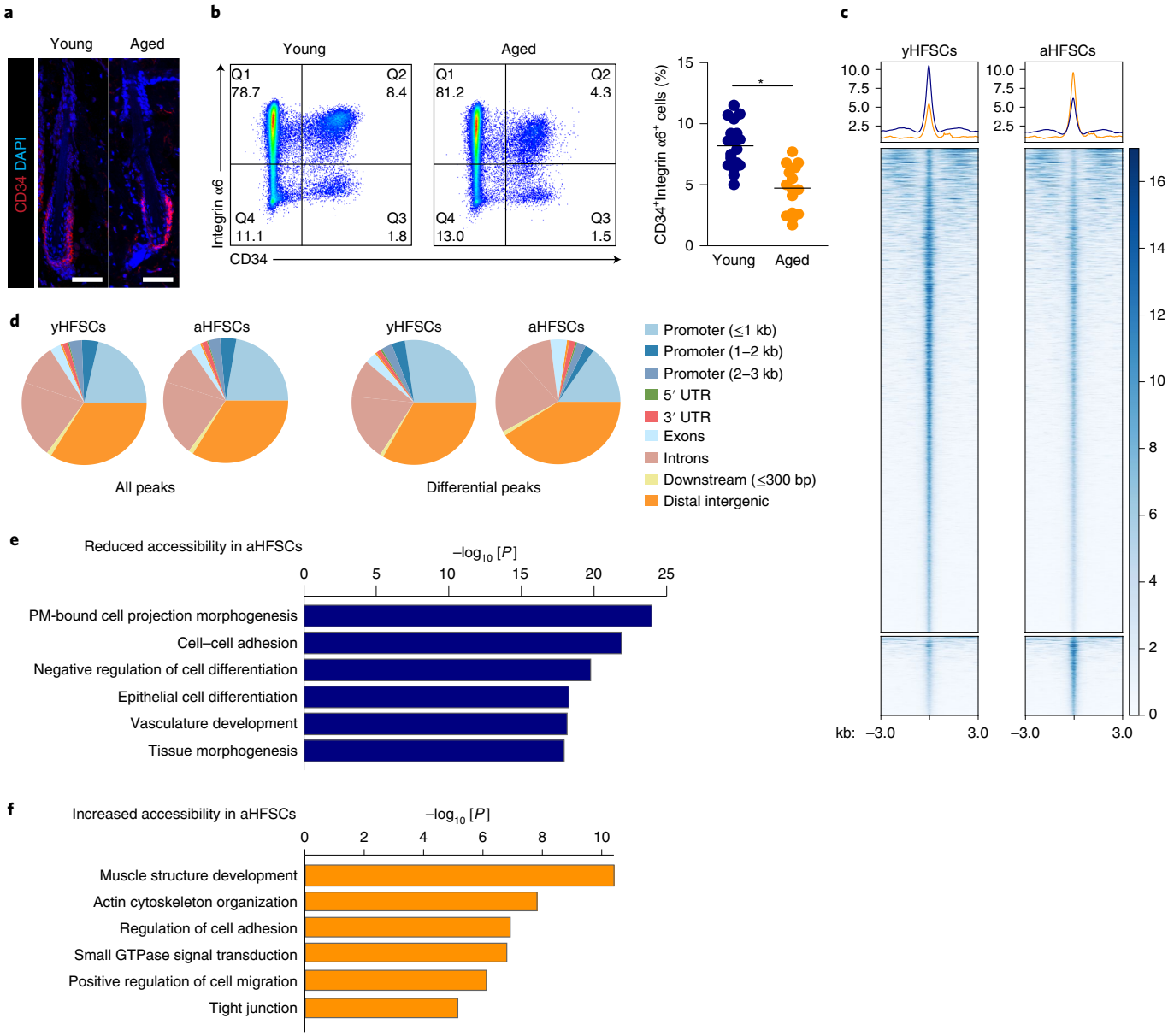

Fig. 1 | Age-induced HFSC exhaustion is associated with decreased chromatin accessibility. a, CD34 (magenta) and nuclear (4′,6-diamidino-2-phenylindole (DAPI); cyan) immunofluorescence images of skin from young adult (aged 12 months) and aged (aged 24 months) mice. Note the comparable hair follicle morphology and the presence of CD34$^+$ HFSCs within the bulge niche. Scale bar, 30 μm. Images representative of $n = 7$ mice per group. **b**, Representative FACS plots and quantification of young and aged epidermal cells stained for CD34 and integrin α6. Quantification of cells (%) in each quadrant (Q) is shown. Note the reduced numbers of CD34$^+$integrin α6$^+$ cells in aged skin. $n = 18$ young and $n = 16$ aged mice. Statistical analysis was performed using a Student's *t*-test; $^*P = 0.0327$. **c**, Heat map and intensity profiles of differentially accessible ATAC-seq peaks. Note the widespread reduction in chromatin accessibility in aged HFSCs (aHFSCs). $n = 4$ mice per group. yHFSCs, young HFSCs. *y* axis labels and colour scale represent reads per genomic content. **d**, Distribution of all (left) and differential (right) ATAC-seq peaks reveals comparable distribution of ATAC-seq peaks in general but increased representation of promoters in regions that are more accessible in young HFSCs and increased representation of intergenic regions in aged HFSCs. **e**,**f**, GO term analyses of peaks that are more accessible in young (**e**) and aged (**f**) HFSCs indicate that developmental and cell differentiation processes are less accessible, whereas genes that are involved in actin cytoskeleton organization and the regulation of cell adhesion are more accessible in aged HFSCs. Statistical analysis was performed using a hypergeometric test with Benjamini-Hochberg correction. UTR, untranslated region. PM, plasma membrane.

numbers[9]. To identify the molecular mechanisms of HFSC ageing, we studied a stage in which the decline in HFSC numbers was visible as a sign of HFSC exhaustion and onset of ageing (24 months), but in which hair follicle morphology and density and the resulting hair coat still appeared to be normal (Fig. 1a and Extended Data Fig. 1a–c). In contrast to previous studies[6–9], we analysed young (6 months) and aged (24 months) mice that were bred at the same facility and housed together in the same room throughout their entire life span. Studies of 3 independent young/aged mouse cohorts from 3 independent mouse colonies/facilities (18 young/16 aged mice in facility 1; Fig. 1b; 7 mice per group in facility 2; and 4 mice per group in facility 3; Extended Data Fig. 1d) confirmed the robust and reproducible age-dependent decline in HFSCs. Importantly, only telogen skin was included in the downstream analyses, and the

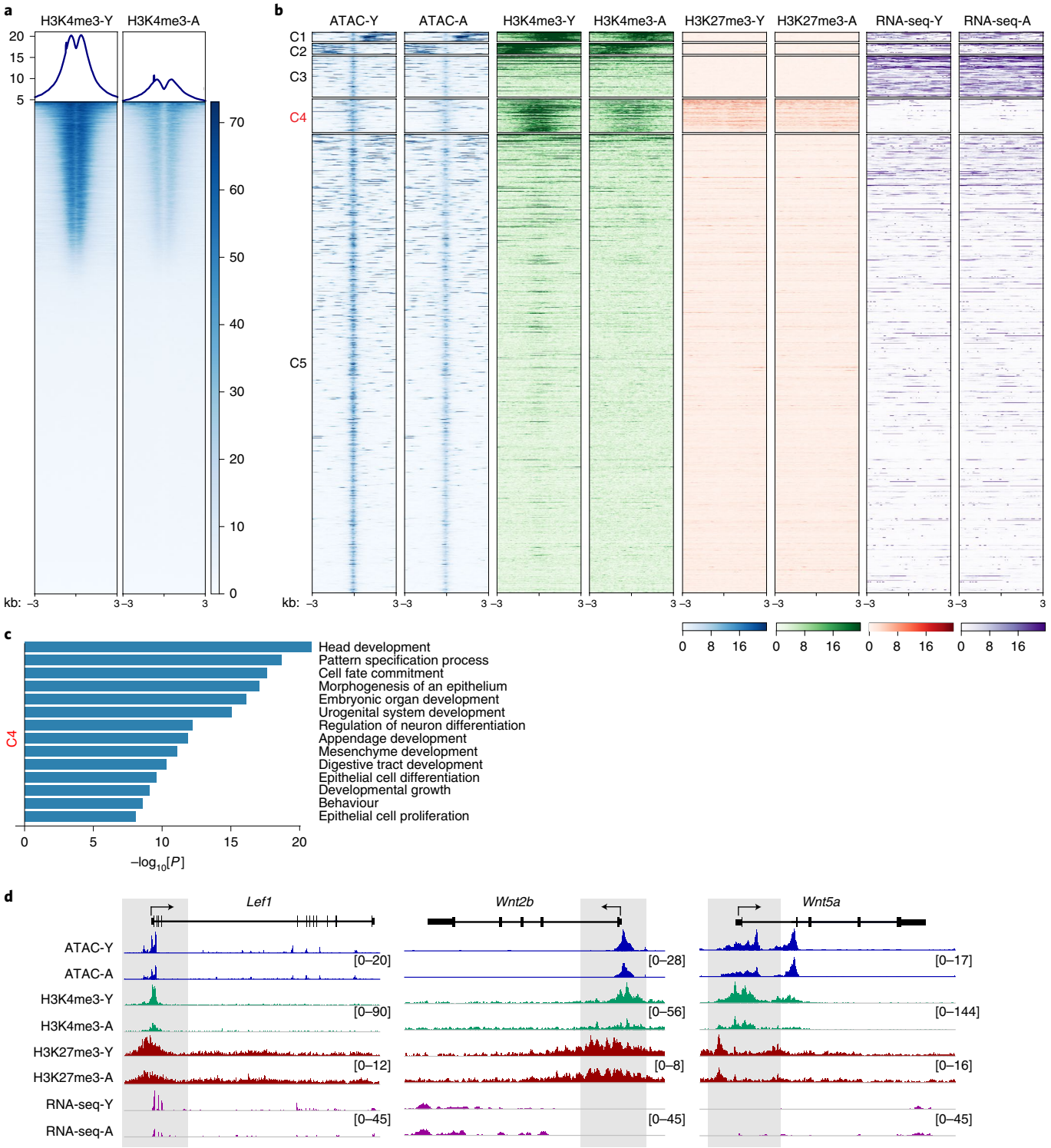

Fig. 2 | HFSC ageing results in the silencing of bivalent promoters. a, Heat map and profile plot of all H3K4me3 peaks from ChIP–seq analysis of young (H3K4me3-Y) and aged (H3K4me3-A) HFSCs shows a reduced peak intensity around aged promoters. $n = 2$ mice per group. *y* axis labels and color scale represent reads per genomic content. **b**, *k*-means clustering of ATAC-seq peaks with decreased accessibility in aged HFSCs on the basis of H3K4me3/H3K27me3 ChIP–seq and RNA-seq data from young and aged HFSCs. Note peak cluster 4 (C4) with both H3K4me3 and H3K27me3 in young HFSCs, the reduced H3K4me3 at these sites in aged HFSCs, and that there are no detectible mRNA transcripts in young or aged HFSCs, indicating a bivalent state with reduced accessibility in aged HFSCs. Color scales represent reads per genomic content. **c**, GO term analyses of the genes found in cluster 4 implicate developmental processes, cell fate and differentiation. Statistical analysis was performed using a hypergeometric test with Benjamini-Hochberg correction. **d**, Representative genome browser views of genes from cluster 4. Peak intensity range is indicated in brackets.

proportion of anagen skin did not correlate with HFSC numbers (Extended Data Fig. 1e), excluding potential prolonged telogen resting phases as the cause of reduced HFSCs in aged mice.

To examine whether epigenetic changes were linked to HFSC exhaustion, we used genome-wide transposase-accessible chromatin sequencing (ATAC-seq)[10] to determine the genome-wide

chromatin accessibility landscape in fluorescence-activated cell sorting (FACS)-purified young and aged HFSCs (4 young and 4 aged mice). All ATAC-seq samples were enriched for reads at transcription start sites (TSSs) and exhibited the expected periodicity of insert length (Fig. 1c,d and Extended Data Fig. 1f). We assessed the differential accessibility between these two groups and discovered that young HFSCs showed significantly more accessible genomic regions compared with aged HFSCs (6,745 in young/1,104 in aged; Fig. 1c). Although the overall distribution of reads was comparable in young and aged HFSCs, the regions with enhanced accessibility in young HFSCs were enriched for promoters and CpG islands, suggesting that accessibility was predominantly reduced at promoters of coding genes in aged HFSCs (Fig. 1d, Extended Data Fig. 1g and Supplementary Table 1). Gene Ontology (GO)-term analyses indicated that genes involved in tissue development and cell differentiation are less accessible in aged HFSCs (Fig. 1e). By contrast, the few regions that were more accessible in aged HFSCs were enriched for transposable elements and intergenic regions (Fig. 1d, Extended Data Fig. 1g and Supplementary Table 1), which are typically silenced by H3K9me3, a modification that is reported to be decreased after ageing[11,12]. Furthermore, processes involved in actin regulation and cell adhesion were enriched among the protein-coding genes with increased accessibility aged HFSCs (Fig. 1f).

Despite these large-scale changes in chromatin accessibility, RNA-sequencing (RNA-seq) analysis of FACS-purified HFSCs revealed relatively minor changes in mRNA expression with only 112 genes upregulated and 227 genes downregulated in aged HFSCs (adjusted P (P_{adj}) < 0.05; Extended Data Fig. 1h and Supplementary Table 2), in agreement with previous studies[13]. Consistent with the ATAC-seq findings, genes downregulated in aged HFSCs represented regulators of cell growth and metabolism, whereas upregulated genes had functions in cell adhesion, cytoskeleton and extracellular matrix (ECM) (Extended Data Fig. 1i). Collectively these data indicate that ageing-induced HFSC exhaustion was associated with decreased chromatin accessibility and gene expression, specifically affecting promoter regions as well as differentiation and certain developmental genes, whereas increased accessibility and expression were observed at intergenic regions and cytoskeletal, adhesion and ECM genes.

Aged HFSCs show silencing of bivalent promoters. To understand the mechanisms and epigenetic context of reduced chromatin accessibility in aged HFSCs, and the absence of substantial corresponding mRNA changes, we first overlaid the ATAC-seq data with published chromatin immunoprecipitation sequencing (ChIP–seq) datasets for H3K4me1, H3K27ac and H3K27me3 from HFSCs[14], and observed that a large majority of the differentially accessible intergenic peaks most likely represented poised or inactive enhancers (Extended Data Fig. 2a). Consistent with the global ATAC-seq analysis, genes closest to the putative enhancer peaks with reduced accessibility in aged HFCSs were enriched for epithelial differentiation and proliferation genes, whereas regions with increased accessibility were, as expected, related to cell adhesion and negative regulation of proliferation (Extended Data Fig. 2b).

To understand the mechanisms of reduced accessibility at promoters, we subsequently performed ChIP–seq analysis of H3K4me3 and H3K27me3, markers for active and silenced transcription, in purified young and aged HFSCs (Fig. 2a and Extended Data Fig. 2c). Consistent with the reduced chromatin accessibility in aged HFSCs, we observed a widespread decrease in the occupancy of H3K4me3 flanking promoters of aged HFSCs (Fig. 2a and Supplementary Table 3). By contrast, H3K27me3 occupancy was slightly increased (Extended Data Fig. 2c and Supplementary Table 4).

Intriguingly, clustering of the ATAC-seq data with H3K4me3 and H3K27me3 ChIP–seq revealed that one major class of regions with reduced accessibility in aged HFSCs contained both H3K4me3 and H3K27me3 marks at the promoters of young HFSCs as a feature of a bivalent domain (cluster 4; Fig. 2b). These genes were not transcribed in either young or aged HFSCs (Fig. 2b and Supplementary Table 2), excluding transcriptional heterogeneity as a cause for both active and silencing marks. Consistent with the decreased accessibility, reduced H3K4me3 was observed particularly at the promoters of these bivalent genes in aged HFSCs, with no substantial change in H3K27me3 (Fig. 2b and Extended Data Fig. 2d). GO-term enrichment analyses revealed that this cluster of differentially accessible, bivalent genes was enriched for developmental and cell-type-specification genes (Fig. 2c), as expected on the basis of studies of bivalent genes in other SCs[4]. A large majority of these genes had CpG-island-containing promoters (116 out of 131) and included key HFSC differentiation genes such as *Lef1* and multiple *Bmp*, *Wnt* and *Tcf* genes, as well as genes involved in SC self-renewal[5] (Fig. 2d and Extended Data Fig. 2e) that are known to be under the control of polycomb repressive complex-2 and H3K27me3 in HFSCs[14].

Collectively, these data indicate that aged HFSCs show reduced chromatin accessibility and H3K4me3 occupancy, particularly at bivalent promoters that control known key HFSC activation and self-renewal genes.

Niche ageing attenuates bivalent gene activation and SC potency. We hypothesized that the age-associated loss of promoter bivalency/accessibility at key proliferation and differentiation genes would compromise the efficient cell-cycle entry that is required for self-renewal as well as the differentiation capacity of aged HFSCs.

Fig. 3 | Ageing leads to niche-dependent compromised activation of bivalent genes and loss of SC potential. a, Schematic of the hair depilation experiment to induce HFSC activation. HFSCs (orange), hair germ (HG) cells (pink) and dermal papilla (DP) fibroblast (grey) are shown. **b**, Representative immunofluorescence image and quantification of 5-ethynyl-2′-deoxyuridine (EdU)$^+$ cells (white arrows) within the hair follicles show efficient cell cycle entry of young HFSCs in contrast to aged. $n = 4$ young and $n = 6$ aged mice. Statistical analysis was performed using a Mann–Whitney U-test; $^{**}P = 0.0095$. Scale bars, 75 µm. **c**, RT–qPCR analysis of selected genes with a bivalent promoter state and reduced accessibility in aged HFSCs after depilation. Note the reduced expression in aged HFSCs/progenitors. $n = 6$ mice per group. Statistical analysis was performed using Mann–Whitney U-tests; $^{**}P = 0.022$. **d**, Representative examples of young and aged mice 5 d after depilation. Note the grey skin of young mice, indicative of the mid-anagen hair follicle growth stage, whereas old skin is pink, indicative of early anagen. **e**,**f**, Representative images (**e**) and quantification (**f**) of the hair follicle stage in young and aged skin 9 d after depilation indicating delayed growth of aged HFCSs ($n = 4$ mice per group with >10 hair follicles per mouse). Scale bars, 50 µm. **g**, Representative images and quantification of total colony number and frequency distribution of colony sizes from purified HFSCs plated in clonal density on feeders. Note the reduced colony-forming ability (left) and loss of small colonies (right) in aged HFSCs. $n = 9$ mice per group. Statistical analysis was performed using Student's t-tests ($^{**}P = 0.0041$; colony number; left) and analysis of variance (ANOVA) with the Holm–Sidak test ($^{*}P = 0.0209$, $^{***}P < 0.0001$; colony size frequency; right). **h**, Schematic of the transplantation experiments. **i**, Representative images and quantification of the hair follicle density of nude mice with transplants of young and aged HFSCs show that young and aged cells have a comparable hair follicle regeneration capacity. $n = 3$ young and $n = 4$ aged donors and corresponding recipients. **j**, Quantification of CD34$^+$integrin α6$^+$ cells from HFSC organoid cultures generated from young and aged epidermis with and without cyclopamine (Cyclo.) treatment. Note the comparable levels of CD34$^+$integrin α6$^+$ cells in cultures from young and aged cells. $n = 4$ donor mice per group. For **c**, data are mean ± s.e.m.; for **f**, **g** and **i**, data are mean ± s.d.

To test this, we first assayed the cycling of HFSCs as a readout for self-renewal. As HFSCs are mostly quiescent, we administered 5-bromo-2′deoxyuridine (BrdU) in drinking water continuously for 8 weeks. During this time, a majority (~70%) of young HFSCs had incorporated BrdU, whereas this was reduced by almost 50% in aged HFSCs (Extended Data Fig. 3a). We next induced in vivo

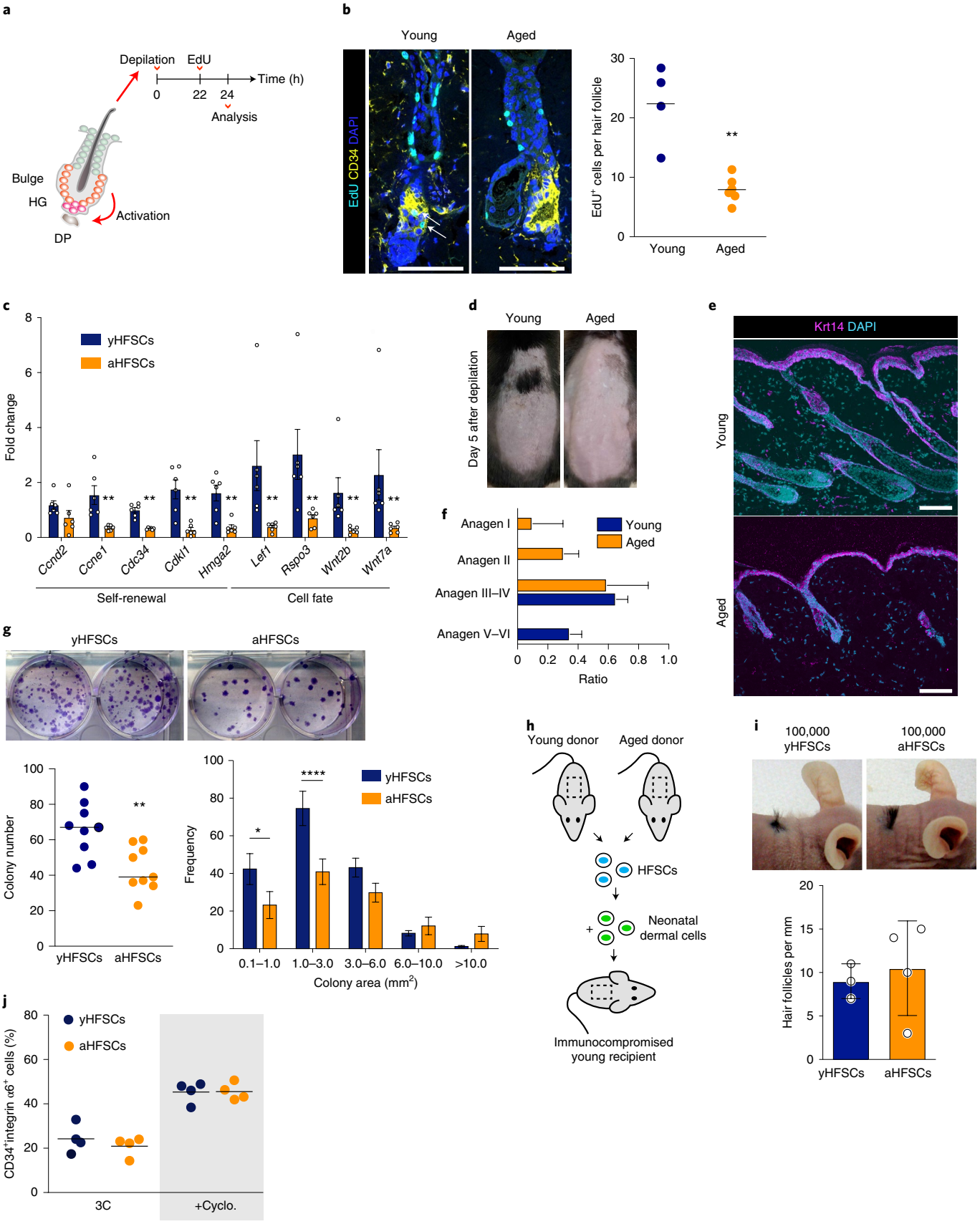

HFSC activation and subsequent hair follicle anagen entry by depilation[15] (Fig. 3a) and observed that young HFSCs were efficiently activated and entered the cell cycle, whereas aged HFSCs showed a substantially attenuated response (Fig. 3b). Importantly, and consistent with efficient cell-cycle entry, bivalent genes were activated by depilation in young HFSCs/progenitors, but this activation was severely compromised in aged cells (Fig. 3c). As a consequence, the reduced HFSC activation substantially delayed anagen entry and progression in aged HFs (Fig. 3d–f; classification according to ref. [16]). The compromised HFSC potency was further confirmed using colony-forming assays. As predicted, aged HSFCs formed substantially fewer colonies than young HFSCs (Fig. 3g). We next functionally assessed the relationship between age-dependent attenuated expression of bivalent genes and compromised HFSC self-renewal. Depletion of *Wnt7a*, *Lef1*, *Cdc34* and *Hmga2* in young HFSCs using siRNA (Extended Data Fig. 3b) decreased the colony-forming potential of these cells (Extended Data Fig. 3c–e), resembling the phenotype of aged HFSCs.

To test whether age-dependent regulation of HFSC epigenetic state and function was cell autonomous or niche-dependent, we transplanted the aged cells into young nude mice (Fig. 3h,i). Strikingly, aged HFSCs were as potent as their young counterparts in regenerating hair (Fig. 3i). Furthermore, aged HFSCs/progeny displayed comparable levels of H3K4me3 as the young cells, indicative of rejuvenation of their epigenetic state (Extended Data Fig. 3f).

These data suggest a role for the niche in the HFSC epigenetic changes and the decrease in SC potency in aged mice. To challenge this hypothesis, we examined the self-renewal and activation potential of young and aged HFSCs in an ex vivo organoid culture system that enables long-term HFSC self-renewal and maintenance[17]. In this system, critical niche components such as EGF, FGF-2 and various laminins and heparan sulfate proteoglycans (Matrigel) are externally provided[17]. Aged HFSCs were again as capable of maintaining their numbers as young HFSCs (Fig. 3j). In response to the Shh inhibitor cyclopamine, which is known to block differentiation[18], young and aged HFSCs further expanded equally, therefore indicating a comparable self-renewal ability (Fig. 3j). Finally, despite the strong reduction in H3K4me3 at bivalent promoters of quiescent HFSCs in aged mice (Fig. 2a,b), placing the cells in organoid cultures facilitated a rapid gain in H3K4me3 at bivalent gene promoters within 24 h, resulting in levels of H3K4me3 that were comparable to in young HFSCs (Extended Data Fig. 3g). As a consequence, similar levels of bivalent gene transcripts were detected in young and aged HFSC organoid cultures (Extended Data Fig. 3h).

Collectively, these experiments revealed that aged HFSCs are compromised in self-renewal, activation potency and activation of bivalent genes. Importantly, these compromised functional SC properties along with the epigenetic state are restored after providing a young niche or a synthetic youthful niche.

ECM alterations induce niche stiffening to control SC potential. To understand which changes in the niche contribute to HFSC ageing, we next determined the whole-skin proteome of young and aged mice (Fig. 4a). This resulted in 3,458 quantified proteins in young and old skin with 440 proteins significantly altered between the two conditions ($P_{adj} < 0.05$, Supplementary Table 5). Strikingly, the most significantly upregulated proteins in aged mice were related to the ECM (collagens VI, VII and XI), basement membrane (BM; laminins and collagen IV), BM crosslinking (Loxl1), as well as cell adhesion and contractility (integrins, Rock1; Fig. 4a,b), in agreement with the observed changes in the RNA and ATAC-seq data. Interestingly, ECM proteins of the dermo–epidermal junction, expressed by the dermal fibroblasts, and associated with skin tensile strength and collagen fibril formation (collagen XIV, SPARC[19,20]), were downregulated (Fig. 4a). In agreement with the increased expression of BM components, electron microscopy analysis of young and old skin samples revealed a thickening of the BM throughout the epidermis and hair follicle (Fig. 4c,d). Furthermore, both laminin 332 and 511 staining was increased in aged BMs (Extended Data Fig. 4a,b), further validating the proteome analysis.

We predicted that the thickening of the BM and the increased levels of ECM proteins and cross-linking enzymes would lead to stiffening of the BM. Indeed, atomic force microscopy-based force indentation spectroscopy experiments showed an increased elastic moduli—that is, an increased resistance of the protein composite to deformation after mechanical stress application—of the aged BM around the hair follicle bulge niche (Fig. 4e).

We next investigated whether an aged, stiffened BM alters SC potency. To test this, we cultured young and aged HFSCs on cell- and soluble-factor-free BMs prepared from young and aged skin for 4 d (Fig. 4f,g and Extended Data Fig. 4c,d). Strikingly, in contrast to young BMs, aged BMs failed to promote proliferation as well as activation/differentiation of both young and aged HFSCs, as assessed by Ki67 and Lef1 staining, respectively (Fig. 4f,g). Thus, altered BM composition and/or mechanics influence HFSC behaviour.

To probe whether matrix stiffness alone is sufficient to control HFSC potency and the activation of bivalent self-renewal and differentiation genes, we modified the HFSC organoid culture system to tune the stiffness of the hydrogels to mimic the stiffness of young and aged BMs (Extended Data Fig. 4e). Intriguingly, and as already observed in the earlier organoid culture experiments, aged and young HFSCs in soft hydrogels matching the range of young BM (1–3 kPa) showed comparable activation of bivalent genes after 72 h of culture. By contrast, increasing hydrogel stiffness to match

Fig. 4 | Widespread biochemical alterations in the ECM induce niche stiffening to control SC potential. a, Significantly altered proteins in young and aged skin. BM components such as laminins and collagen IV and its cross-linker Loxl1 are upregulated in old skin whereas ECM modulators such as Sparc and collagen XIV are downregulated. $n = 4$ mice per group. Statistical analysis was performed using moderated *t*-tests with Benjamini–Hochberg correction; $P_{adj} < 0.05$. **b**, GO-term analysis of differentially expressed proteins indicates that ECM and BM components are the most enriched protein classes. **c**,**d**, Representative electron micrographs (**c**) and quantification (**d**) of BM thickness show thickening of the BM in aged mice. $n = 4$ young and $n = 5$ aged mice. Statistical analysis was performed using a Mann–Whitney *U*-test; $P = 0.0159$. Scale bars, 350 nm. Dashed lines indicate BM, insets show 2× magnification of the images. **e**, Atomic force microscopy force indentation measurements of BM stiffness. Note the increased BM stiffness in aged mice. The top, middle and bottom delimiters show the 75th, 50th and 25th percentiles, and the top and bottom whiskers show the maximum and minimum values. $n = 1{,}000$ force curves pooled across $n = 5$ mice per group. Statistical analysis was performed using a Kolmogorov–Smirnov test; $^{**}P = 0.0079$. **f**, Representative Ki67 and Lef1 immunofluorescence images and quantification in young HFSCs plated on decellularized BM scaffolds derived from young and aged mice. Note the reduced presence of Ki67- and Lef1-positive cells in BM scaffolds from aged mice. $n = 3$ mice per group. Statistical analysis was performed using Student's *t*-tests; $^{**}P = 0.0037$, $^{*}P = 0.044$. Scale bars, 25 µm. **g**, Representative Ki67 and Lef1 immunofluorescence images and quantification in aged HFSCs plated on decellularized BM scaffolds derived from young and aged mice. Note the increased presence of Ki67- and Lef1-positive cells in BM scaffolds from young mice. $n = 4$ donors and recipients per group. Statistical analysis was performed using Mann–Whitney *U*-tests; $^{*}P = 0.0286$. Scale bars, 25 µm. **h**, RT–qPCR analysis of selected bivalent genes in young and aged HFSCs cultured in soft and stiff hydrogels. Note the reduced expression stiff hydrogels. $n = 5$ cultures per group. Statistical analysis was performed using ANOVA and Fisher's Least Significant Difference test. *P* values are indicated on the graph. For **d**, **f** and **g**, data are mean ± s.d.; for **h**, data are mean ± s.e.m.

aged BM (5–6 kPa) was sufficient to mimic the attenuated activation of SC self-renewal and differentiation gene transcription, as seen in aged HFCSs after depilation in vivo, now also in young HFSCs (Fig. 4h).

Thus, ageing induces large-scale changes in the skin ECM and BM that promote stiffening of the HFSC niche. Niche stiffening promotes loss of accessibility and therefore reduced activation of bivalent SC genes, leading to loss of HFSC self-renewing potential.

Increased BM stiffness compromises HFSC maintenance in vivo. Even if age-dependent matrix stiffening is probably a multifactorial phenotype[21], we next investigated whether the individual changes

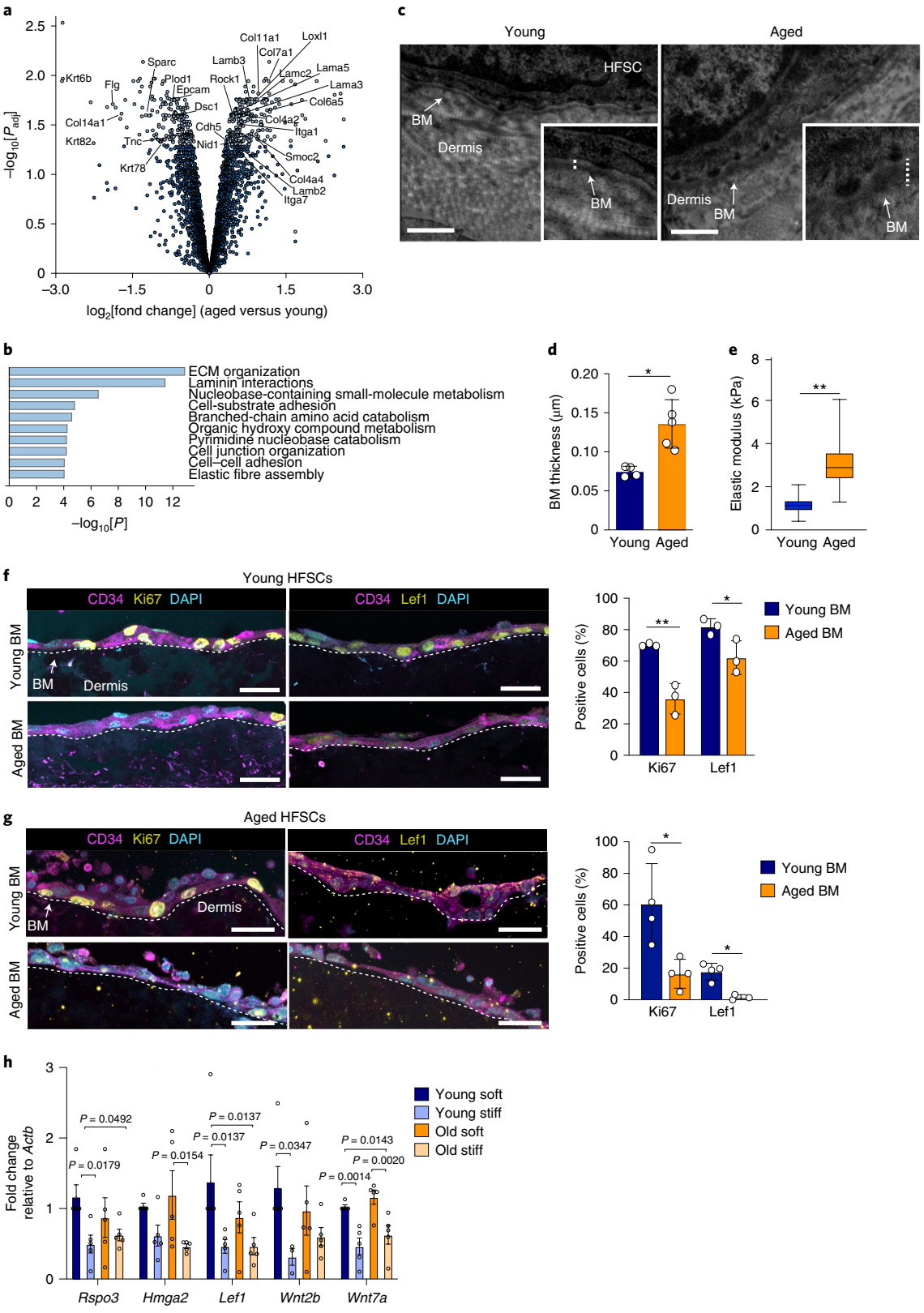

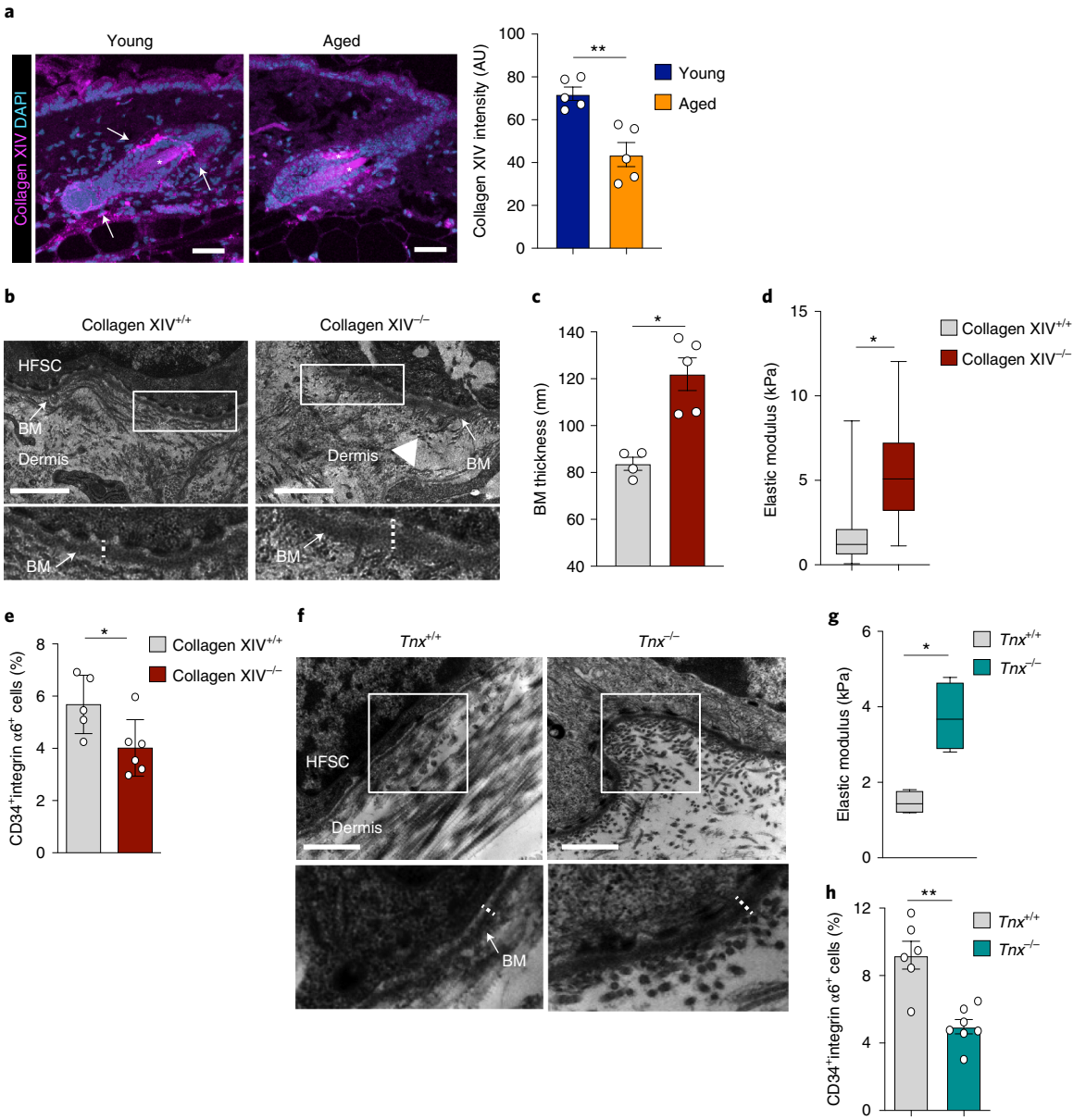

Fig. 5 | Increased BM stiffness compromises HFSC maintenance in vivo. a, Representative collagen XIV immunofluorescence images and quantification in young and aged mice. Note the presence of collagen XIV around the hair follicle bulge (arrows), which is reduced in aged mice. The asterisks mark unspecific signal from hair shaft. $n=5$ mice per group. Statistical analysis was performed using a Student's *t*-test; $^{**}P=0.0079$. Scale bars, 25 µm. **b**,**c**, Representative electron micrographs (**b**) and quantification (**c**) of BM thickness in skin from one-year-old wild-type (collagen XIV$^{+/+}$) and collagen-XIV-deficient (collagen XIV$^{-/-}$) mice. The arrows indicate BM and the arrowheads show disorganized collagen fibres in the dermis. The white rectangles indicate the magnified regions in the bottom images. $n=4$ collagen XIV$^{+/+}$ and $n=5$ collagen XIV$^{-/-}$ mice. Statistical analysis was performed using a Mann–Whitney *U*-test; $^{*}P=0.0159$. Scale bars, 1µm. Insets show 2× magnification of the images. **d**, Atomic force microscopy force indentation measurements of BM stiffness in collagen XIV$^{+/+}$ and collagen XIV$^{-/-}$ mice. Note the increased BM stiffness in collagen XIV$^{-/-}$ mice. $n>20$ force maps pooled across $n=4$ mice per genotype. Statistical analysis was performed using a Kolmogorov–Smirnov test; $^{*}P=0.0286$. **e**, Quantification of CD34^{+}integrin α6^{+} cells from one-year-old collagen XIV$^{+/+}$ and collagen XIV$^{-/-}$ mouse epidermis shows decreased numbers of HFSCs in collagen XIV$^{-/-}$ mice. $n=5$ collagen XIV$^{+/+}$ and $n=6$ collagen XIV$^{-/-}$ mice. Statistical analysis was performed using a Student's *t*-test; $^{*}P=0.0338$. **f**, Representative electron micrographs from wild type (*Tnx*$^{+/+}$) and tenascin-X-deficient (*Tnx*$^{-/-}$) mouse skin. Image representative of $n=3$ mice per genotype. Scale bars, 1µm. Insets show 2× magnification of the images. **g**, Atomic force microscopy force indentation measurements of BM stiffness in *Tnx*$^{+/+}$ and *Tnx*$^{-/-}$ mice. Note the increased BM stiffness in *Tnx*$^{-/-}$ mice. $n=23$ force maps pooled across $n=4$ mice per genotype. Statistical analysis was performed using a Kolmogorov–Smirnov test; $^{*}P=0.0286$. **h**, Quantification of CD34^{+}integrin α6^{+} cells from one-year-old *Tnx*$^{+/+}$ and Tnx$^{-/-}$ mouse epidermis shows decreased numbers of HFSCs in *Tnx*$^{-/-}$ mice. $n=6$ *Tnx*$^{+/+}$ and $n=7$ *Tnx*$^{-/-}$ mice. Statistical analysis was performed using a Student's *t*-test; $^{**}P=0.0026$. Data are mean ± s.d. For the box plots, the top, middle and bottom delimiters show the 75th, 50th, 25th percentiles, and the top and bottom whiskers show the maximum and minimum values, respectively.

in ECM proteins observed in the proteome of aged skin could be sufficient to promote BM stiffening and HFSC depletion in vivo. We focused on collagen XIV as one of the most significantly downregulated ECM proteins in aged skin (Fig. 4a). Moreover, changes in collagen XIV have been associated with aberrant collagen fibrillogenesis in the skin, resulting in a reduced tensile strength

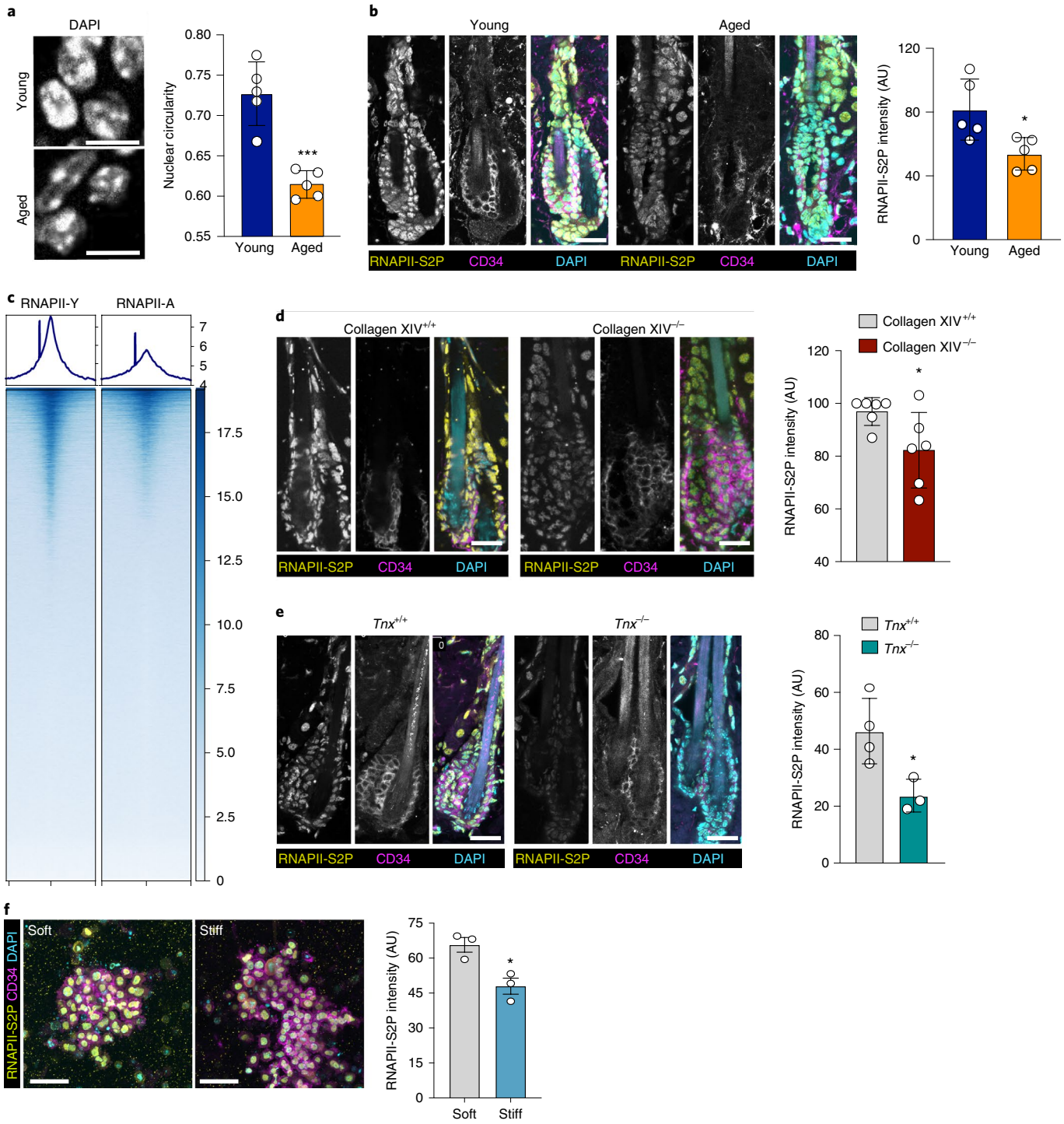

Fig. 6 | Mechanical stress suppresses transcription to silence bivalent promoters. a, Representative immunofluorescence images and quantification of nuclear circularity in young and aged bulge HFSCs. Note the decreased circularity and irregular shapes of aged nuclei. $n=5$ mice per group. Statistical analysis was performed using a Student's *t*-test; $^{***}P=0.0004$. Scale bars, 10 μm. **b**, Representative immunofluorescence images and quantification of RNAPII-S2P in young and aged bulge HFSCs show decreased levels of RNAPII-S2P in aged HFSCs. $n=5$ mice per group. Statistical analysis was performed using a Student's *t*-test; $^{*}P=0.0213$. Scale bars, 25 μm. **c**, RNAPII ChIP–seq analysis of young (RNAPII-Y) and aged (RNAPII-A) HFSCs shows a reduced peak intensity at the promoters in aged HFSCs. *y* axis labels and colour scale represent reads per genomic content. **d**, Representative immunofluorescence images and quantification of RNAPII-S2P in collagen XIV$^{+/+}$ and collagen XIV$^{-/-}$ mice shows decreased levels of RNAPII-S2P in collagen XIV$^{-/-}$ hair follicle bulges. $n=6$ mice per genotype. Statistical analysis was performed using a Student's *t*-test; $^{*}P=0.0405$. Scale bars, 25 μm. **e**, Representative immunofluorescence images and quantification of RNAPII-S2P in *Tnx*$^{+/+}$ and *Tnx*$^{-/-}$ mice shows decreased levels of RNAPII-S2P in *Tnx*$^{-/-}$ hair follicle bulges. $n=4$ (*Tnx*$^{+/+}$) and $n=3$ (*Tnx*$^{-/-}$) mice. Statistical analysis was performed using a Student's *t*-test; $^{*}P=0.0273$. Scale bars, 25 μm. **f**, Representative immunofluorescence images and quantification of RNAPII-S2P in HFSC organoids in soft and stiff hydrogels show decreased levels of RNAPII-S2P in stiff hydrogels. $n=3$ independent experiments with more than 400 cells per condition per experiment. Statistical analysis was performed using a Student's *t*-test; $^{*}P=0.0192$. Scale bars, 25 μm. For **a**, **b** and **d**–**f**, data are mean ± s.d.

of connective tissue, a phenomenon that is also found in ageing[19,22]. Immunofluorescence analyses confirmed the decreased collagen XIV levels in aged skin and further revealed a specific enrichment of collagen XIV at the dermal–epidermal junction around the hair follicles of young mice (Fig. 5a). To directly investigate whether the loss of collagen XIV accelerates ageing-dependent changes in HFSC function, we examined one-year-old collagen-XIV-deficient mice. This analysis revealed that, similar to the aged (two-year-old) wild-type mice (Fig. 1a and Extended Data Fig. 1a), there were no large-scale morphological abnormalities within the epidermis or the hair follicles of one-year-old collagen-XIV-deficient mice (Extended Data Fig. 5a,b). However, analysis of the dermal–epidermal junction revealed disorganization of sub-BM collagen fibres in the one-year-old collagen-XIV-deficient mice, as expected[19], alongside substantial BM thickening and stiffening of the BM (Fig. 5b–d), comparable to two-year-old wild-type mice. Most importantly, collagen-XIV-deficient mice showed a premature decline in HFSC numbers already at one year of age (Fig. 5e and Extended Data Fig. 5c). Thus, the phenotype of one-year-old collagen-XIV-deficient mice closely resembled the phenotype of the two-year-old aged wild-type mice, indicative of a premature skin ageing phenotype.

To examine whether changes in collagen matrix mechanics are the cause of BM stiffening and HFSC depletion or whether specific collagen-XIV-related molecular changes are required, we also analysed mice deficient for tenascin-X, an ECM protein that is not significantly altered in aged skin. This protein is involved in collagen fibre stabilization and is mutated in human Ehlers–Danlos Syndrome, which is characterized by defective organization of dermal collagen fibres and increased macroscopic hyperelasticity of the skin, indicative of altered mechanical properties of the dermis[23]. Tenascin-X-knockout mice displayed a substantially thickened and stiff BM (Fig. 5f,g and Extended Data Fig. 5d) and a premature progressive decline in HFSC numbers (Fig. 5h and Extended Data Fig. 5e–g), similar to collagen-XIV-deficient mice. Together these experiments show that impairing matrix organization at the dermal–epidermal junction is associated with increased BM thickness and stiffness, leading to premature HFSC exhaustion.

Mechanical stress reduces transcription to silence bivalent promoters. We next sought to unravel the molecular mechanisms by which age-induced niche stiffening controls promoter states and thereby HFSC potency. We predicted that increased stiffening of the BM would enhance mechanosignalling and perhaps cause mechanical stress in aged HFSCs. Cell contractility as quantified by the levels of myosin-II phosphorylation[24] was increased in aged HFSCs (Extended Data Fig. 6a), consistent with the observed upregulation of its upstream kinase Rock1 in the proteomics data (Fig. 4a). Together with data from the ATAC and RNA-seq analyses that showed increased accessibility and expression of cytoskeletal and cell adhesion genes (Fig. 1 and Extended Data Fig. 1), these data indicated increased mechanosignalling in aged HFSCs. Moreover, quantification of the nuclear shape in young and aged HFSC niches revealed increased nuclear flattening and shape heterogeneity in aged HFSCs (Fig. 6a and Extended Data Fig. 6b)—a further indication of mechanical stress.

We have previously demonstrated that mechanical stress leads to global transcriptional repression and a decreased presence of the active, elongating form of RNA polymerase 2 (serine-2-phosphorylated form; RNAPII-S2P)[25]. Consistent with the increase in mechanical stress in the aged HFSCs, we observed a notable decrease in RNAPII-S2P immunofluorescence in aged bulge HFSCs (Fig. 6b). This was further confirmed by ChIP–seq, which showed genome-wide reduction of RNAPII occupancy in aged HFSCs (Fig. 6c and Supplementary Table 6). Importantly, a similar decrease in RNAPII-S2P was also detected both in one-year-old collagen-XIV- and tenascin-X-deficient mouse HFSCs in vivo (Fig. 6d,e), as well as in organoids cultured in stiff hydrogels (Fig. 6f), therefore demonstrating a key role for niche mechanics in attenuating transcription. By contrast, increasing H3K4me3 levels in HFSC organoids by inhibiting Kdm5—a H3K4me3 demethylase[26]—did not substantially further increase the transcriptional levels of the group of bivalent genes (Extended Data Fig. 6c,d), suggesting that increases in H3K4me3 mark rather than actively promote the expression of these genes, at least once they have been activated.

Collectively these analyses show that stiffening of the niche microenvironment reduces transcription, which ultimately leads to the silencing of bivalent genes.

Discussion

Collectively, our results demonstrate that ageing reduces chromatin accessibility of HFSCs, particularly at bivalent lineage-specification genes. This specific chromatin state is influenced by transcriptional activity that is suppressed by the increased, niche-derived mechanical stress that acts on the aged HFSCs. Thus, the microenvironment and its mechanical properties have a critical role in regulating the SC chromatin landscape and functionality during ageing.

An important contribution of cell non-autonomous factors in SC is starting to emerge. A role of systemic factors mammalian SC ageing has already been demonstrated, for example, in muscle satellite cells and in the skin epidermis through heterochronic parabiosis whereby young systemic factors enhanced aged SC regenerative capacity[27,28]. Focusing on the local microenvironment, recent research in the skin epidermis reported altered ECM expression concomitant with compromised HFSC mobilization after wound healing in aged mice, but not after transplantation into young recipients[13]. Consistent with this previous research, we now identify that increased niche stiffness, resulting from the changes in ECM composition and most likely cross-linking, is a critical factor that drives HFSC ageing by promoting the silencing of bivalent genes that are critical for HFSC activation. The precise mechanism that triggers BM stiffening in aged mice is probably multifactorial and remains open for future studies. However, our findings showing that multiple components of the dermal–epidermal junction, such as collagen XIV, are reduced in aged skin, and that genetic manipulation of collagen XIV or tenascin X leads to reduced tensile strength of the bulk tissue[19,23] and, in the long-term, to increased BM thickness and stiffness, lead us to postulate that increased mechanical stress at the dermal–epidermal junction, as a result of weakening of the collagen supramolecular assembly, triggers compensatory changes within the BM as an attempt to stabilize the tissue. This abnormally stiff BM negatively impacts the state of HFSCs, preventing their efficient self-renewal and activation in aged tissue. Given that the absence of tenascin X results in Ehlers–Danlos Syndrome in humans, it is intriguing to note that a subset of these patients displays features of premature ageing in their skin such as hair loss, epidermal thinning and translucency[29].

Interestingly, increased tissue stiffening has been shown to impact oligodendrocyte progenitor cell ageing in the central nervous system[30], indicating that altered niche mechanics probably represent a general driver of SC ageing. It will be interesting to assess whether the decrease in promoter accessibility is a unifying mechanism of stiffness-driven SC functional decline across cell types.

Online content

Any methods, additional references, Nature Research reporting summaries, source data, extended data, supplementary information, acknowledgements, peer review information; details of author contributions and competing interests; and statements of data and code availability are available at https://doi.org/10.1038/s41556-021-00705-x.

Received: 6 April 2020; Accepted: 27 May 2021;
Published online: 8 July 2021

References

1. Lopez-Otin, C., Blasco, M. A., Partridge, L., Serrano, M. & Kroemer, G. The hallmarks of aging. *Cell* **153**, 1194–1217 (2013).
2. Signer, R. A. & Morrison, S. J. Mechanisms that regulate stem cell aging and life span. *Cell Stem Cell* **12**, 152–165 (2013).
3. Voigt, P., Tee, W. W. & Reinberg, D. A double take on bivalent promoters. *Genes Dev.* **27**, 1318–1338 (2013).
4. Harikumar, A. & Meshorer, E. Chromatin remodeling and bivalent histone modifications in embryonic stem cells. *EMBO Rep.* **16**, 1609–1619 (2015).
5. Hsu, Y. C., Li, L. & Fuchs, E. Emerging interactions between skin stem cells and their niches. *Nat. Med.* **20**, 847–856 (2014).
6. Doles, J., Storer, M., Cozzuto, L., Roma, G. & Keyes, W. M. Age-associated inflammation inhibits epidermal stem cell function. *Genes Dev.* **26**, 2144–2153 (2012).
7. Giangreco, A., Qin, M., Pintar, J. E. & Watt, F. M. Epidermal stem cells are retained in vivo throughout skin aging. *Aging Cell* **7**, 250–259 (2008).
8. Keyes, B. E. et al. Nfatc1 orchestrates aging in hair follicle stem cells. *Proc. Natl Acad. Sci. USA* **110**, E4950-9 (2013).
9. Matsumura, H. et al. Hair follicle aging is driven by transepidermal elimination of stem cells via COL17A1 proteolysis. *Science* **351**, aad4395 (2016).
10. Buenrostro, J. D., Giresi, P. G., Zaba, L. C., Chang, H. Y. & Greenleaf, W. J. Transposition of native chromatin for fast and sensitive epigenomic profiling of open chromatin, DNA-binding proteins and nucleosome position. *Nat. Methods* **10**, 1213–1218 (2013).
11. Saha, P. & Mishra, R. K. Heterochromatic hues of transcription—the diverse roles of noncoding transcripts from constitutive heterochromatin. *FEBS J.* **286**, 4626–4641 (2019).
12. Brunet, A. & Rando, T. A. Interaction between epigenetic and metabolism in aging stem cells. *Curr. Opin. Cell Biol.* **45**, 1–7 (2017).
13. Ge, Y. et al. The aging skin microenvironment dictates stem cell behavior. *Proc. Natl Acad. Sci. USA* **117**, 5339–5350 (2020).
14. Lien, W. H. et al. Genome-wide maps of histone modifications unwind in vivo chromatin states of the hair follicle lineage. *Cell Stem Cell* **9**, 219–232 (2011).
15. Ito, M., Kizawa, K., Hamada, K. & Cotsarelis, G. Hair follicle stem cells in the lower bulge form the secondary germ, a biochemically distinct but functionally equivalent progenitor cell population, at the termination of catagen. *Differ. Res. Biol. diversity* **72**, 548–557 (2004).
16. Muller-Rover, S. et al. A comprehensive guide for the accurate classification of murine hair follicles in distinct hair cycle stages. *J. Invest. Dermatol.* **117**, 3–15 (2001).
17. Chacon-Martinez, C. A., Klose, M., Niemann, C., Glauche, I. & Wickstrom, S. A. Hair follicle stem cell cultures reveal self-organizing plasticity of stem cells and their progeny. *EMBO J.* **36**, 151–164 (2017).
18. Hsu, Y. C., Li, L. & Fuchs, E. Transit-amplifying cells orchestrate stem cell activity and tissue regeneration. *Cell* **157**, 935–949 (2014).
19. Ansorge, H. L. et al. Type XIV collagen regulates fibrillogenesis: premature collagen fibril growth and tissue dysfunction in null mice. *J. Biol. Chem.* **284**, 8427–8438 (2009).
20. Bradshaw, A. D. et al. SPARC-null mice display abnormalities in the dermis characterized by decreased collagen fibril diameter and reduced tensile strength. *J. Invest. Dermatol.* **120**, 949–955 (2003).
21. Guimaraes, C. F., Gasperini, L., Marques, A. P. & Reis, R. L. The stiffness of living tissues and its implications for tissue engineering. *Nat. Rev. Mater.* **5**, 351–370 (2020).
22. Langton, A. K., Graham, H. K., Griffiths, C. E. M. & Watson, R. E. B. Ageing significantly impacts the biomechanical function and structural composition of skin. *Exp. Dermatol.* **28**, 981–984 (2019).
23. Mao, J. R. et al. Tenascin-X deficiency mimics Ehlers-Danlos syndrome in mice through alteration of collagen deposition. *Nat. Genet.* **30**, 421–425 (2002).
24. Murrell, M., Oakes, P. W., Lenz, M. & Gardel, M. L. Forcing cells into shape: the mechanics of actomyosin contractility. *Nat. Rev. Mol. Cell Biol.* **16**, 486–498 (2015).
25. Le, H. Q. et al. Mechanical regulation of transcription controls Polycomb-mediated gene silencing during lineage commitment. *Nat. Cell Biol.* **18**, 864–875 (2016).
26. Vinogradova, M. et al. An inhibitor of KDM5 demethylases reduces survival of drug-tolerant cancer cells. *Nat. Chem. Biol.* **12**, 531–538 (2016).
27. Conboy, I. M. et al. Rejuvenation of aged progenitor cells by exposure to a young systemic environment. *Nature* **433**, 760–764 (2005).
28. Nishiguchi, M. A., Spencer, C. A., Leung, D. H. & Leung, T. H. Aging suppresses skin-derived circulating SDF1 to promote full-thickness tissue regeneration. *Cell Rep.* **24**, 3383–3392 (2018).
29. Sarbacher, C. A. & Halper, J. T. Connective tissue and age-related diseases. *Subcell. Biochem.* **91**, 281–310 (2019).
30. Segel, M. et al. Niche stiffness underlies the ageing of central nervous system progenitor cells. *Nature* **573**, 130–134 (2019).

Methods

Mice. Wild type C56Bl6/J mice were used for ageing experiments. Male mice aged 24–30 weeks were used as the young group (~6 months) and male mice aged 100–110 weeks (~24 months) were used as the aged group. Collagen-XIV- and tenascin-X-deficient mice have been reported previously[19,23]. Telogen stage mice (aged 45–55 d) were used for keratinocyte isolation. All of the animals in the same experimental groups were bread at the same animal facility and housed in the same room. All of the animal experiments were approved by authorities of North Rhine Westphalia, Germany (licences 84-02.04.2014.A491 and 2014.A478).

Flow cytometry. For freshly isolated epidermal cells, single-cell suspensions were generated by incubating skin pieces in 0.8% trypsin for 50 min. For organoids, Matrigel droplets were degraded for 8 min at 37 °C using 0.5% trypsin and 0.5 mM EDTA in PBS.

Trypsin was neutralized using FACS buffer (2 mM EDTA and 2% fetal bovine serum in PBS). Cells were then pelleted by centrifugation for 5 min at 2,000 r.p.m. at 4 °C, resuspended in FACS buffer and stained with anti-CD34-eFluor 660 (Thermo Fisher Scientific, 50-0341-82, 1:100) and anti-ITGA6-eFluor 450 (Thermo Fisher Scientific, 48-0495-82, 1:300) antibodies on ice. 7AAD (Thermo Fisher Scientific) for live/dead cell detection was added to each sample 15 min before the analysis. Cells were analysed using the FACSCanto II (BD Biosciences) system or sorted using FACSAria Illu Svea (BD Biosciences) and/or FACSAria Fusion (BD Biosciences) systems. Sorted cells were collected into tubes with cell culture medium at 4 °C, centrifuged, and either snap-frozen in liquid nitrogen or resuspended in medium and cultured. Data were analysed using FlowJo (v.5.0; BD Biosciences). The gating strategy used is shown in Supplementary Fig. 1.

Immunofluorescence and confocal microscopy. For paraffin sections tissue biopsies were fixed (4% paraformaldehyde (PFA)), embedded in paraffin and sectioned. Sections were deparaffinized using a graded alcohol series and antigen retrieval was performed using Target Retrieval Solution (Dako) pH 6 or pH 9 in a pressure cooker. For cryosections, tissues were placed unfixed into OCT Tissue Tek and frozen on dry ice. Then, 6–8-µm-thick sections were cut and fixed with 4% PFA. For both paraffin and cryosections, samples were blocked in 10% goat serum, and incubated with primary antibodies diluted in DAKO antibody diluent overnight at 4 °C. Bound primary antibodies were detected by incubation with Alexa Fluor 488-, 568- or 647-conjugated antibodies (Invitrogen). Nuclei were counterstained with DAPI (Invitrogen). Slides were mounted in Elvanol. The following antibodies were used: anti-CD34 (Thermo Fisher Scientific, 14-0341-82, 1:100), anti-Sox9 (Santa Cruz, sc-20095, 1:100), anti-keratin-15 (Thermo Fisher Scientific, MS-1068, 1:300), anti-pMLC2 (Cell Signaling, 3674, 1:100), anti-RNA polymerase II phospho-S2 (Abcam ab5095, 1:900), anti-Ki67 (Abcam ab15580, 1:1000), anti-Lef1 (Cell Signaling, 2230, 1:100), anti-E-cadherin (BD Biosciences 610181, 1:300), anti-laminin 332 (gift from R. E. Burgeson[31]; 1:20,000), anti-laminin α5 (504; gift from L. Sorokin[32]; 1:20,000), anti-H3K4me3 (Cell Signaling, 9727, 1:300) and anti-collagen XIV[19] (1:5,000).

Images were collected by laser scanning confocal microscopy (SP8X; Leica) with the Leica Application Suite software (LAS X, v.2.0.0.14332) using a ×40 immersion objective. Images were acquired at room temperature using sequential scanning of frames of 1-µm-thick confocal planes (pinhole 1) after which the planes were projected as a maximum intensity confocal stack. Images were collected with the same settings for all of the samples within an experiment.

BrdU feeding. For long term in vivo proliferation assays, mice were fed with 0.5 mg ml^{-1} of the thymidine homologue BrdU in drinking water continuously for 8 weeks. Tissue samples were collected and BrdU was detected from paraffin sections using an anti-BrdU antibody (BD Biosciences, 347580; 1:50) as described above.

Image analyses. Images were analysed using Fiji[33] (v.2.0.0). Fields were randomly selected exclusively on the basis of the presence of nuclei, as assessed by DAPI staining. For quantification, areas of interest were generated using automated thresholding of the DAPI staining or manually around specific anatomical structures, after which mean fluorescence intensities were quantified within the areas of interest from maximum projection images obtained as described above.

H&E staining. Tissues were fixed in 4% PFA for 1 h on ice and embedded in paraffin as described above. Subsequently, haematoxylin and eosin (H&E) staining was performed using the automated Gemini slide stainer (Thermo Fisher Scientific). Stained tissues were mounted onto coverslips with Cytoseal XYL mounting medium (Thermo Fisher Scientific). Images of H&E-stained tissue samples were obtained using the Nikon Eclipse Ci (Nikon) ×20 air objective and NIS Elements D software (v.4.51, Nikon).

HFSC organoids and hydrogels. Epidermal cells were isolated from telogen-stage mice and cultured in 3C organoid conditions as described previously[17]. In brief, single-cell suspensions were generated by incubating skin pieces in 0.8% trypsin for 50 min. Cells were suspended in growth-factor-reduced Matrigel (Corning) and grown in 3C medium (MEM Spinner's modification (Sigma-Aldrich), 5 µg ml^{-1} insulin (Sigma-Aldrich), 10 ng ml^{-1} EGF (Sigma-Aldrich), 10 µg ml^{-1} transferrin (Sigma-Aldrich), 10 µM phosphoethanolamine (Sigma-Aldrich), 10 µM ethanolamine (Sigma-Aldrich), 0.36 µg ml^{-1} hydrocortisone (Calbiochem), 2 mM glutamine (Gibco), 100 U ml^{-1} penicillin and 100 µg ml^{-1} streptomycin (Gibco), and 10% chelated fetal calf serum (Gibco), 5 µM Y27632, 20 ng ml^{-1} mouse recombinant VEGF and 20 ng ml^{-1} human recombinant FGF-2 (all from Miltenyi Biotec)). Where indicated, cells were treated with the Kdm5 inhibitor CPI-455 (26 µM; Selleckchem) for 6 d.

For organoids in soft and stiff hydrogels, PEG-cross-linked collagen hydrogels were generated essentially as described previously[34]. Collagen I (Millipore, 08-115) was mixed with reconstitution buffer (0.26 M sodium hydrogen carbonate, 0.2 M HEPES, 0.05 N sodium hydroxide and 1× Hank's Balanced salt solution (Sigma-Aldrich, H1641)), and cells in 3C medium at a ratio of 4:1:7 to yield a final collagen I concentration of 1.6 mg ml^{-1}. To tune stiffness, PEG-diNHS (Sigma-Aldrich, E3257; molecular mass, 456.36) was dissolved in dimethyl sulfoxide (DMSO) at a concentration of 50 mg ml^{-1}. The solution was then added to the collagen per cell mixture at a final 0.17 PEG-diNHS-to-collagen mass ratio. The hydrogel–cell mixtures (80,000 cells per droplet) were allowed to polymerize at 37 °C for 1 h and then cultured in 3C medium. The elastic moduli of the hydrogels were validated using atomic force microscopy as described below.

ATAC-seq and analyses. ATAC-seq libraries were prepared as previously described[10]. In brief, nuclei of 50,000 freshly FACS-sorted single HFSCs were prepared by lysing cells with cold lysis buffer (10 mM Tris-HCl, pH 7.4, 10 mM NaCl, 3 mM $MgCl_2$ and 0.1% IGEPAL CA-630) for 15 min on ice. Nuclei were then collected by centrifuging at 6,000*g* for 10 min at 4 °C, resuspended in Tagment DNA Buffer and Tagment DNA Enzyme (TruSight One Kit) and incubated for 30 min at 37 °C. The samples were purified using the MinElute PCR purification kit (Qiagen) and PCR-amplified with 10–12 cycles. The concentration and quality of libraries were confirmed using the D1000 Tape Station (Agilent) before sequencing. Libraries were paired-end sequenced with the 2×75bp protocol using the Illumina HiSeq4000 system according to manufacturer's instructions.

Adapters were trimmed using Flexbar (v.2.5)[35] and reads were aligned against the GRCm38.81 mouse genome using BWA MEM (v.0.7.12)[36] using the standard parameters. Differential peaks were called and analysed using THOR (v.0.1)[37]. DeepTools (v.3.3.1)[38] was used to calculate correlation between samples, normalize reads to 1× depth of coverage and generate heat maps. Sequencing tracks were visualized using the Integrative Genomics Viewer (v.2.4.14)[39]. Annotation of peaks and GO analysis were performed using Homer (v.4.10)[40]. GO term analyses were performed using Homer and Metascape[41]. Genomic annotations were visualized using ChIPseeker (v.1.2.6)[42]. ChIP datasets on H3K4me1, H3K27me3 and H3K27ac in HFSCs were downloaded from GSE31239 to compare differential ATAC-seq peaks with chromatin features. These datasets were mapped similarly as described above. Heat maps of the ChIP–seq signal over the differential peak regions were then generated with Deeptools and split into five clusters using the *k*-means algorithm. Clusters were annotated and analysed with Homer and Metascape.

RNA-seq and analyses. HFSCs were FACS purified from epidermis as described above. Total RNA was isolated using the NucleoSpin RNA Plus kit (Macherey&Nagel). After quantification and quality control using the Agilent 2200 TapeStation, total RNA amounts were adjusted and libraries were prepared using the Ovation RNA-Seq System V2 (NuGen) followed by subsequent library preparation using the Nextera XT library preparation kit (Illumina). Paired-end RNA-seq was performed using Illumina HiSeq3000 machines with the 2×150-bp protocol. After quality control, adapter sequences were removed using Flexbar[36]. After preprocessing, reads were mapped to the mouse reference genome build GRCm38.p5 using STAR (v.2.5.2b)[43]. Gene expression was subsequently estimated using featureCounts (v.1.6.2)[44]. FeatureCounts results were aggregated over all samples and differential gene expression was calculated using the R package DEseq2 (v.1.22.2)[45].

Chromatin immunoprecipitation sequencing and analyses. H3K4me3, H3K27me3 and Pol2 ChIP–Seq experiments were performed using Diagenode's ChIPmentation Kit for Histones (C01011010). In brief, HFSCs were FACS-purified from epidermis as described above. Cells were cross-linked with 0.25% methanol-free formaldehyde (Thermo Fisher Scientific, 28906) for 10 min at room temperature. Fixation was terminated by adding 0.125 M glycine in PBS for 5 min. Cells were subsequently washed with PBS after which cells were pelleted by centrifugation at 5,000 r.p.m. for 10 min at 4 °C. Cell pellets were lysed through 10 strokes of Dounce homogenization. Lysates were sonicated using a Covaris M20 sonicator (4–9 °C temperature range; 15% duty factor 75% peak power) for 10 min. After sonication, the samples were centrifuged at 21,000*g* for 5 min at 4 °C and the supernatant was collected as the chromatin fraction. DNA concentration was measured using the Qubit DS high-sensitivity kit (Invitrogen) and sample concentrations were adjusted to be equal. Ten percent of chromatin was collected as input and 2 µl was analysed using the Agilent 2200 TapeStation to ensure optimal shearing (300–600 bp fragments), and the rest was analysed using immunoprecipitation. For this, sheared chromatin, DiaMag Protein A-coated beads and 3 µg of antibodies (anti-H3K27me3, Active motif, 39155; anti-H3K4me3, Cell

Signaling, 9727; or anti-Pol2, Cell Signaling, 14958) were combined to a ChIP reaction mix and incubated overnight at 4 °C. Beads were collected using a magnet, washed, resuspended in tagmentation buffer containing 1 µl of tagmentation enzyme and incubated for 10 min at 37 °C. After several washes, bound complexes were released from beads, end-repaired and cross-linking was reversed. The optimal cycle number for library amplification was determined by qPCR and libraries prepared for sequencing by PCR using barcoded primer sets. Libraries were pooled and sequenced on the Illumina HiSeq 2000 sequencer using the 100 bp paired-end setting.

Adapters were trimmed using Flexbar (v.2.5)[36] and reads were aligned against the GRCm38.81 mouse genome using BWA MEM (v.0.7.12)[37] with the standard parameters. DeepTools (v.3.3.1)[39] was used to calculate correlation between samples, normalize reads to 1× depth of coverage and generate heat maps. Sequencing tracks were visualized with Integrative Genomics Viewer (v.2.4.14)[40]. Macs2 (v.2.2.7.1)[46] was used to call peaks and DiffBind (v.2.14.0)[47] for the differential analysis of consensus peaks. For the comparison of H3K4me3 at bivalent and other promoters, the $\log_2$-transformed fold change of differential promoters was calculated by DiffBind.

Chromatin immunoprecipitation qPCR. Chromatin was cross-linked and processed as described above. Subsequently, 380 µl of ChIP dilution buffer (20 mM Tris-HCl pH 8.1, 2 mM EDTA, 150 mM NaCl and 1% Triton X-100) and 3 µg of antibody (anti-H3K4me3, Cell Signaling, 9727; or IgG control, Cell Signaling, 5415) were added and the samples were incubated in an end-over mixer for 16 h at 4 °C. Protein G Dynabeads (30 µl) were subsequently added to each sample and further rotated in an end-over mixer for 4 h at 4 °C. Beads were collected using a magnet and washed once with ChIP dilution buffer, followed by washes in wash buffer 1 (50 mM HEPES pH 7.9, 500 mM NaCl, 1 mM EDTA, 1% Triton X-100, 0.1% Na-deoxycholate, 0.1% SDS), wash buffer 2 (20 mM Tris pH 8.0, 1 mM EDTA, 250 mM LiCl, 0.5% NP-40, 0.5% Na-deoxycholate) and finally with 20 mM Tris pH 8.0, 1 mM EDTA. Samples were subsequently eluted in 50 mM Tris pH 8.0, 0.1 mM EDTA, 1% SDS at 65 °C for 30 min. To reverse cross-links, 8 µl 1 M NaCl and 5 µl of 20 mg ml^{-1} proteinase K were added to the samples, which were then incubated first for 3 h at 42 °C and then at 65 °C for 16 h. Subsequently, 10 mg ml^{-1} RNase A was added for 2 h 37 °C. DNA was purified by phenol–chloroform extraction, followed by ethanol precipitation, after which DNA content was quantified using Qubit. Samples were analysed by qPCR with primers listed in Supplementary Table 7.

Quantification of anagen and telogen area. Mice were euthanized, shaved thoroughly and photographed. The surface area ratios of dark skin areas representing anagen and light skin areas representing telogen were quantified from the back skin using Fiji.

Electron microscopy. Skin samples were isolated and fixed overnight at 4 °C with 4% PFA and 2% glutaraldehyde in 0.1 M sodium cacodylate buffer, pH 6.2. Samples were then rinsed with 0.1 M sodium cacodylate buffer pH 6.2, stained with 1% uranyl acetate and incubated in 70% ethanol. After dehydration through an ethanol series, samples were embedded in araldite resin. Ultrathin (30–70 nm) sections were cut with a diamond knife using an ultramicrotome and placed onto copper grids for transmission electron microscopy (TEM). TEM was performed using a Zeiss 902A electron microscope (Zeiss). Images were acquired using the Megaview III Soft Imaging System camera and analySIS software (Soft Imaging System).

Colony-forming assay. J2 feeder cells (ATCC) were treated with 0.5 mg ml^{-1} mitomycin C in DMEM with 10% fetal bovine serum and penicillin–streptomycin for 2 h at 37 °C. HFSCs were isolated from the mice using flow cytometry as described above and plated at a low clonal density (10^3 cells per well on a 6-well plate) on mitomycin C-treated J2 feeders and cultured for 3–4 weeks in FAD medium (DMEM + Ham's F12 with 5 µg ml^{-1} insulin, 10 ng ml^{-1} EGF, 1.8×10^{-4} M adenin, 0.5 µg ml^{-1} hydrocortisone, 10% chelated fetal calf serum (FCS), 10^{-10} M choleratoxin). Colonies were fixed with 4% PFA and subsequently stained with 0.1% crystal violet and quantified.

RNAi. HFSCs were isolated and expanded in organoid cultures as described above. After 10 d of culture, transfections were performed in two dimensions using Lipofectamine RNAiMAX (Thermo Fisher Scientific) according to the manufacturer's instructions. Then, 72 h after transfection, single-cell suspensions were generated and seeded onto J2 feeder cells for colony-forming analysis as described above. The following Silencer Select predesigned siRNAs (Thermo Fisher Scientific) were used: *Hmga2* siRNA (s67600), *Lef1* siRNA (s69161), *Cdc34* siRNA (s103506), *Wnt7a* siRNA (s76098), negative control siRNA (4404021).

Mass spectrometry. Back skin of mice (200 mg wet weight) was snap-frozen in liquid nitrogen and crushed using a mortar and pestle. Samples were resuspended in guanidinium chloride reduction and alkylation buffer (6 M guanidinium chloride, 20 mM tris(2-carboxyethyl)phosphine, 80 mM chloroacetamide, 100 mM Tris pH 8.5), boiled for 10 min and subsequently mixed (6 times for 30 s, cooled on ice in between) using a FastPrep-24 instrument (MP Biomedicals). Lysates were sonicated using the Bioruptor sonicator (Diagenode) (15 cycles of 30 s) and diluted with 25 mM Tris, pH 8.5. Subsequently, 200 µg of protein was digested overnight with Lys-C (Promega, VA1170) and Trypsin-Gold (Promega, V5280) at a 1:50 ratio at 37 °C. The samples were then sonicated again and further digested for 3 h with Lys-C and trypsin (1:100 ratio). After digestion, the samples were acidified to block trypsin and peptides were cleaned using custom-packed C18-SD STAGE tips[48]. Then, 4 µg of desalted peptides were labelled with tandem mass tags (TMT10plex, Thermo Fisher Scientific, 90110) using a 1:20 ratio of peptides to TMT reagent. TMT labelling was performed according to the manufacturer's instructions with the following changes: dried peptides were reconstituted in 9 µl 0.1 M TEAB to which 7 µl TMT reagent in acetonitrile (ACN) was added to a final ACN concentration of 43.75%, after 60 min of incubation at room temperature the reaction was quenched with 2 µl 5% hydroxylamine. Labelled peptides were pooled, dried, resuspended in 0.1% formic acid (FA), split into two samples and desalted using custom-made C18 STAGE tips[48]. One out of the two samples was fractionated on a 150 mm, 300 µm, 2 µm C18, AcclaimPepMap (Thermo Fisher Scientific, 164537) column using an Ultimate 3000 system (Thermo Fisher Scientific) at 30 °C. Buffer A was 5% acetonitrile 0.01 M ammonium bicarbonate, buffer B was 80% acetonitrile 0.01 M ammonium bicarbonate. Separation was performed using a segmented gradient from 1% to 50% buffer B, for 90 min and 50% to 95% for 20 min with a flow rate of 4 µl min^{-1}. Fractions were collected every 150 s and combined into nine fractions by pooling every ninth fraction. Pooled fractions were dried using the Concentrator plus (Eppendorf), resuspended in 2 µl 0.1% FA for mass spectrometric analysis. Peptides were separated on a 50 cm, 75 µm Acclaim PepMap column (Thermo Fisher Scientific, 164942) using a 120 min linear, 6% to 31% buffer B; buffer A was 0.1% FA, buffer B was 0.1% FA and 80% ACN. The column was maintained at 50 °C. Eluting peptides were analysed on an Orbitrap Lumos Tribrid mass spectrometer (Thermo Fisher Scientific). Synchronous precursor selection-based MS3 was used for TMT reporter ion signal measurements. Proteomics data were analysed using MaxQuant (v.1.5.2.8)[49]. Differential expression analysis was performed using limma (v.3.34.9)[50] in R. The raw data and the data analysis workflow and results have been deposited at the ProteomeXchange Consortium through the PRIDE partner repository[51] under the dataset identifier PXD018352.

Atomic force microscopy. Atomic force microscopy measurements of hair follicle BMs were performed on freshly cut 16 µm cryosections using the JPK NanoWizard 2 (Bruker Nano) atomic force microscope mounted on an Olympus IX73 inverted fluorescent microscope (Olympus) and operated using the JPK SPM control software (v.5). Cryosections were equilibrated in PBS supplemented with protease inhibitors and measurements were performed within 20 min of thawing the samples. Triangular non-conductive Silicon Nitride cantilevers (MLCT, Bruker Daltonics) with a nominal spring constant of 0.01 N m^{-1} were used for the nanoindentation experiments of the apical surface of cells and the nucleus. For all of the indentation experiments, forces of up to 3 nN were applied, and the velocities of cantilever approach and retraction were kept constant at 2 µm s^{-1}, ensuring an indentation depth of 500 nm. All analyses were performed using JPK data processing software (Bruker Nano). Before fitting the Hertz model corrected by the tip geometry to obtain Young's Modulus (Poisson's ratio of 0.5), the offset was removed from the baseline, the contact point was identified, and cantilever bending was subtracted from all force curves.

qPCR. RNA was isolated using the RNeasy Plus Mini Kit or the RNeasy Plus Micro Kit (Qiagen). RNA was reverse transcribed using the SuperScript VILO Master Mix (Thermo Fisher Scientific) according to the manufacturer's protocol. PCR was performed using the CFX384 Touch Real Time PCR Detection System (Bio-Rad) using the PowerUp SYBR Green Mastermix (Thermo Fisher Scientific). Gene expression was quantified using the $\Delta\Delta C_t$ method with normalization to *Actb*. All of the primers were designed to span exons. A list of the primer sequences is provided in Supplementary Table 7.

Transplantation experiments. Female nude mice (aged 8 weeks; CAnN.Cg-Foxn1nu/Crl BALB/c-nude; Jackson Laboratory) were used as recipients for the transplantation experiments. Nude mice were anaesthetized by injecting ketamine (7 mg ml^{-1}) and xylazine (2 mg ml^{-1}) intraperitoneally (i.p.) followed by an i.p. injection of an analgesic (rimadyl; 0.5 mg ml^{-1}). A small incision was made onto the back skin where silicon transplantation chambers (Renner) were subsequently carefully inserted. Fibroblasts (5×10^6) isolated from new-born mice were mixed with freshly isolated HFSCs (5×10^5) in 100 µl of keratinocyte growth medium (KGM) and injected into the transplantation chamber. Next, 7 d after transplantation, the chambers were carefully removed under anaesthesia. Mice were euthanized 8 weeks after transplantation and tissue biopsies were taken for histology.

Depilation experiments. Mice were anaesthetized with isoflurane, wax was applied on the dorsal skin and the hairs were plucked off using hair removal strips. Then, 22 h after depilation, mice were injected i.p. with EdU (50 mg kg^{-1} bodyweight) and 24 h or 9 d after depilation tissue biopsies were collected for histological analyses and FACS sorting followed by qPCR as described above.

Skin decellularization. The back skin of mice was shaved and the remaining hair was removed using depilation cream. Then, 2 cm × 2 cm pieces were dissected and incubated in 0.02% trypsin 0.5 mM EDTA for 2 h at 37 °C to remove cells. Biopsies were then washed three times in DMEM, 10% FCS to neutralize trypsin and subsequently incubated in 3% Triton X-100 for 3 h and then in 4% sodium deoxycholate for 3 h on a shaker. After three washes in DMEM, 10% FCS biopsies were transferred to 24-well culture inserts (Merck, PIHP01250). HFSCs (1×10^6) were added into the inserts, centrifuged briefly and cultured for 2 d in 3C medium. Biopsies were subsequently switched to 1 mM calcium in 3C medium and cultured for another 2 d before fixation in 4% PFA and immunofluorescence.

Statistics and reproducibility. Statistical analyses were performed using GraphPad Prism (GraphPad, v.8). Statistical significance was determined by the specific tests indicated in the corresponding figure legends. Only two-tailed tests were used. In all cases in which a test for normally distributed data was used, normal distribution was confirmed using D'Agostino–Pearson or Shapiro–Wilk tests ($\alpha = 0.05$). All experiments presented in the manuscript were repeated at least in three independent experiments/biological replicates.

Reporting Summary. Further information on research design is available in the Nature Research Reporting Summary linked to this article.

Data availability

Sequencing data that support the findings of this study have been deposited at the Gene Expression Omnibus (GEO) under the accession code GSE148619. Proteomics data have been deposited to the ProteomeXchange Consortium through the PRIDE partner repository[51] under the dataset identifier PXD018352. Previously published sequencing data[14] that were reanalysed here are available under the accession code GSE31239. Source data are provided with this paper. All other data supporting the findings of this study are available from the corresponding author on reasonable request.

References

31. Marinkovich, M. P., Lunstrum, G. P. & Burgeson, R. E. The anchoring filament protein kalinin is synthesized and secreted as a high molecular weight precursor. *J. Biol. Chem.* **267**, 17900–17906 (1992).
32. Sorokin, L. M. et al. Laminin α4 and integrin α6 are upregulated in regenerating dy/dy skeletal muscle: comparative expression of laminin and integrin isoforms in muscles regenerating after crush injury. *Exp. Cell Res.* **256**, 500–514 (2000).
33. Schindelin, J. et al. Fiji: an open-source platform for biological-image analysis. *Nat. Methods* **9**, 676–682 (2012).
34. Liang, Y. et al. A cell-instructive hydrogel to regulate malignancy of 3D tumor spheroids with matrix rigidity. *Biomaterials* **32**, 9308–9315 (2011).
35. Dodt, M., Roehr, J. T., Ahmed, R. & Dieterich, C. FLEXBAR-flexible barcode and adapter processing for next-generation sequencing platforms. *Biology* **1**, 895–905 (2012).
36. Li, H. Aligning sequence reads, clone sequences and assembly contigs with BWA-MEM. Preprint at https://arxiv.org/abs/1303.3997 (2013).
37. Allhoff, M., Sere, K., J, F. P., Zenke, M. & I, G. C. Differential peak calling of ChIP-seq signals with replicates with THOR. *Nucleic Acids Res.* **44**, e153 (2016).
38. Ramirez, F. et al. deepTools2: a next generation web server for deep-sequencing data analysis. *Nucleic Acids Res.* **44**, W160–W165 (2016).
39. Robinson, J. T. et al. Integrative genomics viewer. *Nat. Biotechnol.* **29**, 24–26 (2011).
40. Heinz, S. et al. Simple combinations of lineage-determining transcription factors prime *cis*-regulatory elements required for macrophage and B cell identities. *Mol. Cell* **38**, 576–589 (2010).
41. Zhou, Y. et al. Metascape provides a biologist-oriented resource for the analysis of systems-level datasets. *Nat. Commun.* **10**, 1523 (2019).
42. Yu, G., Wang, L. G. & He, Q. Y. ChIPseeker: an R/Bioconductor package for ChIP peak annotation, comparison and visualization. *Bioinformatics* **31**, 2382–2383 (2015).
43. Dobin, A. et al. STAR: ultrafast universal RNA-seq aligner. *Bioinformatics* **29**, 15–21 (2013).
44. Liao, Y., Smyth, G. K. & Shi, W. featureCounts: an efficient general purpose program for assigning sequence reads to genomic features. *Bioinformatics* **30**, 923–930 (2014).
45. Love, M. I., Huber, W. & Anders, S. Moderated estimation of fold change and dispersion for RNA-seq data with DESeq2. *Genome Biol.* **15**, 550 (2014).
46. Zhang, Y. et al. Model-based analysis of ChIP-Seq (MACS). *Genome Biol.* **9**, R137 (2008).
47. Ross-Innes, C. S. et al. Differential oestrogen receptor binding is associated with clinical outcome in breast cancer. *Nature* **481**, 389–393 (2012).
48. Rappsilber, J., Ishihama, Y. & Mann, M. Stop and go extraction tips for matrix-assisted laser desorption/ionization, nanoelectrospray, and LC/MS sample pretreatment in proteomics. *Anal. Chem.* **75**, 663–670 (2003).
49. Cox, J. & Mann, M. MaxQuant enables high peptide identification rates, individualized p.p.b.-range mass accuracies and proteome-wide protein quantification. *Nat. Biotechnol.* **26**, 1367–1372 (2008).
50. Ritchie, M. E. et al. limma powers differential expression analyses for RNA-sequencing and microarray studies. *Nucleic Acids Res.* **43**, e47 (2015).
51. Perez-Riverol, Y. et al. The PRIDE database and related tools and resources in 2019: improving support for quantification data. *Nucleic Acids Res.* **47**, D442–D450 (2019).

Acknowledgements

We thank A. M. Luoto and N. Hachenberg for expert technical assistance; A. Gyenis for help with experiments; M. Loparic and D. Schneider for initial atomic force microscopy measurements; L. Sorokin for laminin antibodies; the staff at the FACS & Imaging Facility of MPI for Biology of Ageing, the Imaging Facility of CECAD Cologne and the Biomedicum Helsinki Imaging Unit for imaging support; and C. Becker and E. Kirstat at the Cologne Center for Genomics for help with sequencing. This work was supported by the Sigrid Juselius Foundation, Helsinki Institute of Life Science, Wihuri Research Institute, Max Planck Society, the Max Planck Förderstiftung and the European Research Council (ERC) under the EU Horizon 2020 research and innovation programme (grant agreement 770877—STEMpop) (all to S.A.W.) and the Deutsche Forschungsgemeinschaft (DFG; project number 73111208—SFB 829 (to S.A.W., C.M.N. and A.R.-I.), and FOR2722 to M.K. Y.A.M. is the recipient of the EMBO Long-Term fellowship ALTF 728-2017 and Human Frontier Science Program fellowship LT000861/2018.

Author contributions

J.K. designed and performed most of the experiments and analysed data. Y.A.M. performed atomic force microscopy, immunostainings, organoid experiments, designed experiments and analysed data. S.G. performed the HFSC quantification and BrdU feeding experiments. C.A.C.-M. performed cell sorting and depilation experiments with J.K. J.M. performed immunostainings. X.L. and I.A. performed proteomics experiments. W.B. performed electron microscopy. J.A. performed ChIP sequencing. D.E.B. and M.K. provided collagen XIV and *Tnx* mutant mice and other key reagents. M.B. and A.R.-I. supported the ATAC-seq experiments and analysis of sequencing data. C.M.N. and A.R.-I. designed experiments and analysed data. S.A.W. conceived and supervised the study, designed experiments, analysed data and wrote the paper. All of the authors commented and edited the manuscript.

Competing interests

The authors declare no competing interests.

Additional information

Extended data is available for this paper at https://doi.org/10.1038/s41556-021-00705-x.

Supplementary information The online version contains supplementary material available at https://doi.org/10.1038/s41556-021-00705-x.

Correspondence and requests for materials should be addressed to S.A.W.

Peer review information *Nature Cell Biology* thanks Karl Lenhard Rudolph and the other, anonymous, reviewer(s) for their contribution to the peer review of this work. Peer reviewer reports are available.

Reprints and permissions information is available at www.nature.com/reprints.

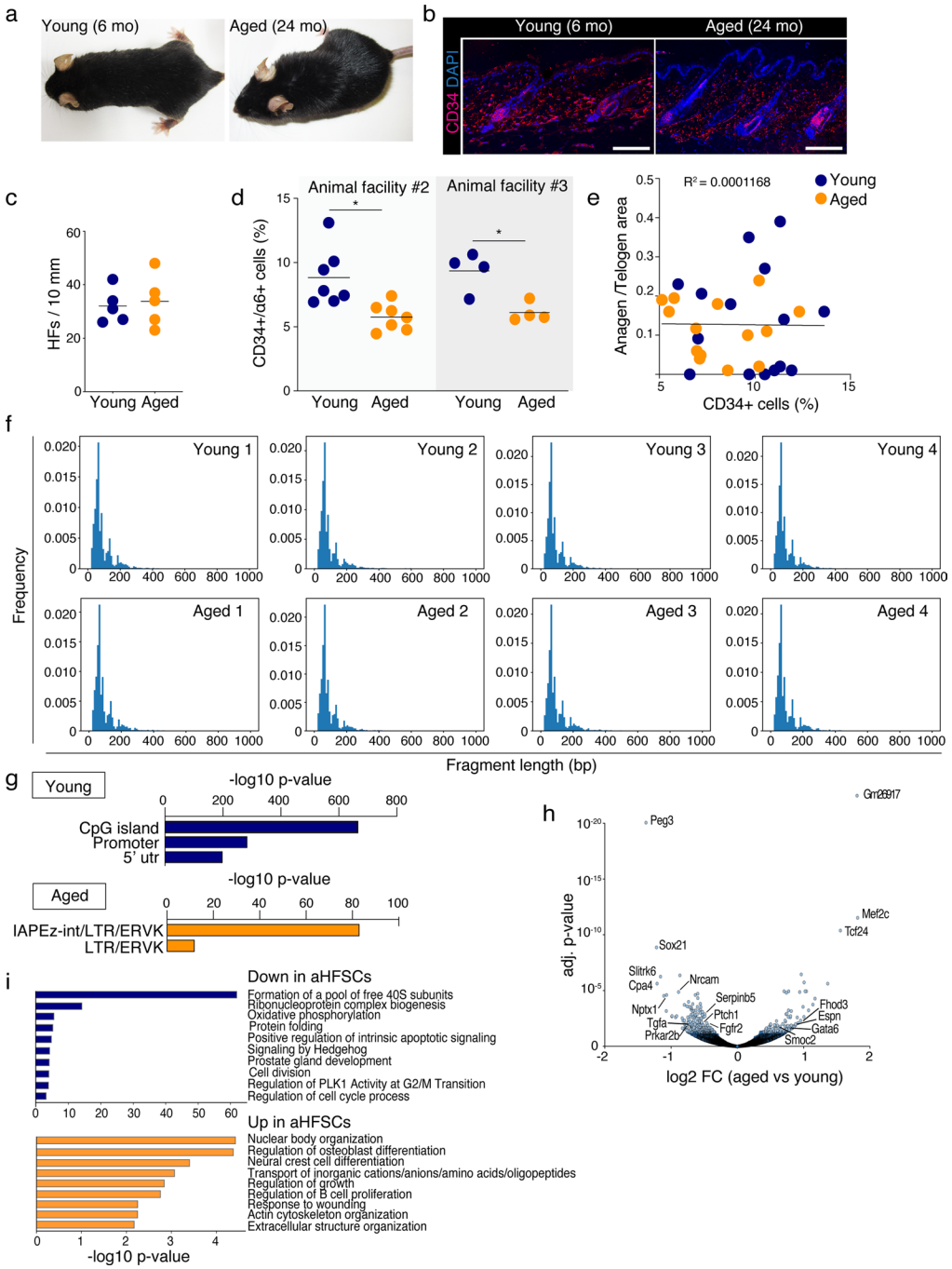

Extended Data Fig. 1 | Analyses of young and aged HFSCs using flow cytometry, ATACseq and RNAseq. a, Representative images of young (6 month) and aged (24 month) old mice show no visible differences in haircoats. (**b,c**) Immunofluorescence imaging (b) and quantification (c) of hair follicle density from young and old mice (mean ±SD; n = 5 mice/group). Scale bars 100 µm. **d**, Quantification of CD34+/α6 integrin+ HFSCs by flow cytometry from young and aged mice cohorts from two different animal facilities (facilities #2 and #3, facility #1 shown in main Fig. 1b), where the respective young and aged mice were housed in the same room. Note decreased HFSC levels in mice from both facilities (mean, n = 7 mice/group; *p = 0.0293 Student's t-test (facility #2), n = 4 mice/group; *p = 0.0283, Mann-Whitney (facility #3)). **e**, Plotting relative abundance of CD34 + HFSCs as a function of anagen-to-telogen ratio shows no correlation between the two parameters in young or aged mice (n = 15 young/14 aged mice; $R^2 = 0.0001168$, Pearson's correlation). **f**, Fragment frequency distribution of the ATACseq reads shows expected distribution both in young and aged biological replicates (n = 4 mice/group). **g**, Motif enrichment analyses of differentially accessible ATACseq peaks shows enrichment of CpG islands and promoter regions in regions more accessible in young HFSCs, whereas more accessible peaks in aged HFSCs are enriched in transposable elements. (-log(p) values: CpG islands - yHFSCs: 670.48/ aHFSCs: 2.03; promoters - yHFSCs: 289.13, aHFSCs: 1.22; 5' utr - yHFSCs: 203.36, aHFSCs: 2.69; IAPEz-int|LTR | ERVK - young HFSCs: -40.18, aged HFSCs: 83.66; LTR | ERVK - young HFSCs: -151.31, aged HFSCs: 12.56) (**h**) Volcano plot of significantly altered transcripts in young and aged HFSCs. Genes involved in differentiation (eg. Mef2c, Gata6, Sox21, Tcf24), proliferation and signaling (Ptch1, Fgfr2, Tgfa, Nptx1), actin cytoskeleton (Espn, Fhod3, Smoc2), and stemness (Peg3) are among the most regulated (n = 3 mice/group; padj<0.05, Wald test/Benjamini-Hochberg). (**i**) GO-term analyses of genes up- and down-regulated in aged HFSCs.

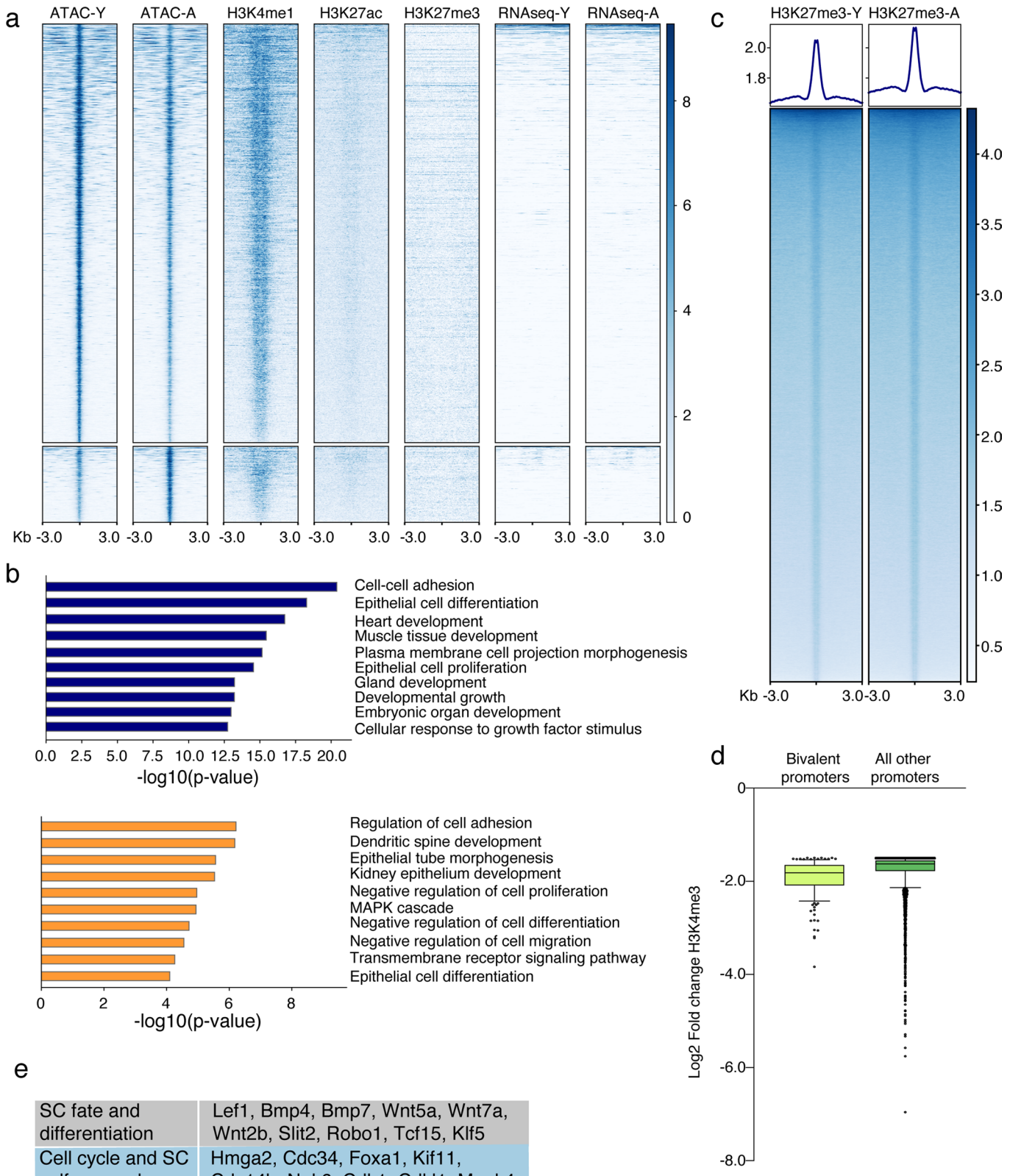

SC fate and differentiation	Lef1, Bmp4, Bmp7, Wnt5a, Wnt7a, Wnt2b, Slit2, Robo1, Tcf15, Klf5
Cell cycle and SC self-renewal	Hmga2, Cdc34, Foxa1, Kif11, Cdc14b, Nek6, Cdk1, Cdkl1, Mapk4

Extended Data Fig. 2 | See next page for caption.

Extended Data Fig. 2 | Histone methylation analyses of young and aged HFSCs. a, Heatmap of differentially accessible intergenic regions clustered according to H3K4me1, H3K27ac, H3K27me3 as well as the transcripts of these regions quantified by RNAseq from young and aged HFSCs. Note that most regions have high H3K4me1, but low H3K27ac and no detectible transcripts, indicative of a primed enhancer state. **b**, GO term analyses of the regions in (a) implicate enhancers for genes involved processes such as cell-cell adhesion, tissue development, cell differentiation, and proliferation to be less accessible (upper panel), whereas enhancers for genes involved in actin cytoskeleton organization and regulation of cell adhesion are more accessible (lower panel) in aged HFSCs. **c**, Heatmap of H3K27me3 ChIP sequencing peaks from young (H3K27me3-Y) and aged (H3K27me3-A) HFSCs shows slightly increased peak intensity in aged HFSCs (n = 2 mice/group). **d**, Box plot of -log2 fold changes of H3K4me3 occupancy at promoters of aged HFSC compared to young (top, middle and bottom delimiters are the 75th, 50th, 25th percentiles; top and bottom whiskers are the 90th and 10th percentiles; n = 2 mice/group). **e**, Representative genes from cluster-4 with functions in stem cell (SC) fate, differentiation and self-renewal include key genes required for HFSC activation and differentiation.

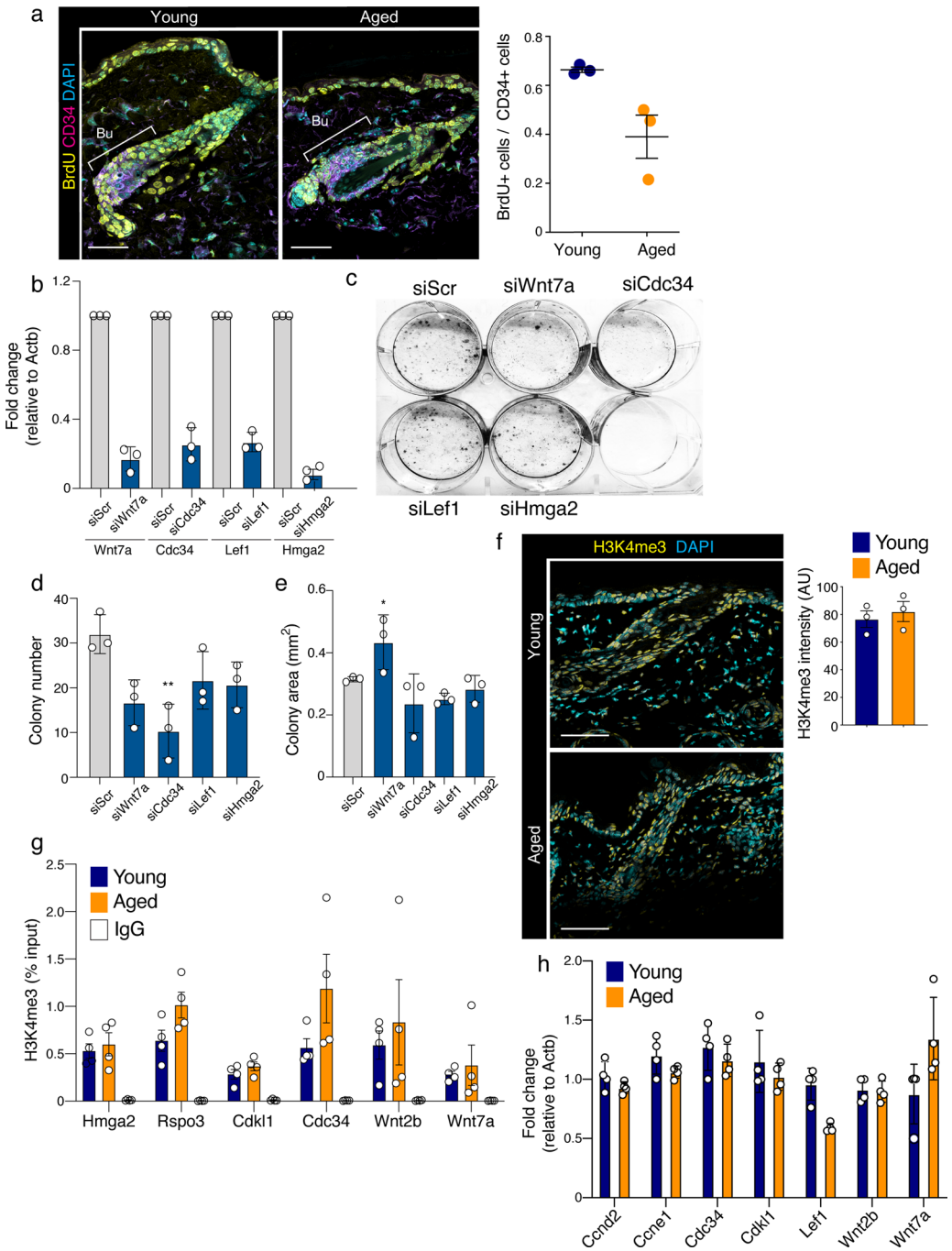

Extended Data Fig. 3 | Niche-dependent regulation of HFSC potency and epigenetic state. a, Representative images and quantification of BrdU incorporation in bulge (Bu) HFSCs from mice fed with BrdU in drinking water for 4 weeks. Note reduced BrdU incorporation in aged HFSCs (n = 3 mice/group). Scale bars 25 µm. **b**, Quantitative RT-PCR of RNAi knockdowns for selected genes with bivalent promoter state (n = 3 independent experiments). (**c**-**e**) Representative images (**c**) and quantification of colony number (**d**) and size (**e**) from colony forming assays with HFSCs depleted of the indicated genes (n = 3 independent experiments; *p = 0.0263, RM-ANOVA/Fischer's, **p = 0.0045, Friedman/Dunn's). **f**, Representative images and quantification of H3K4me3 in hair follicles generated in young nude mice by transplanting young or aged HFSCs (n = 3 mice/group). Scale bars 25 µm. **g**, Quantitative RT-PCR of selected genes with bivalent promoter state and reduced accessibility in vivo from H3K4me3 ChIP of young and aged HFSCs in 24 h 3 C organoid cultures. No significant differences in expression are observed (n = 4 mice/group). **h**, Quantitative RT-PCR of selected genes with bivalent promoter state and reduced accessibility in vivo from young and aged HFSCs in 3 C organoid cultures. No significant differences in expression are observed (n = 4 mice/group). Bar graphs in g, h show mean ±SEM, others mean ±SD.

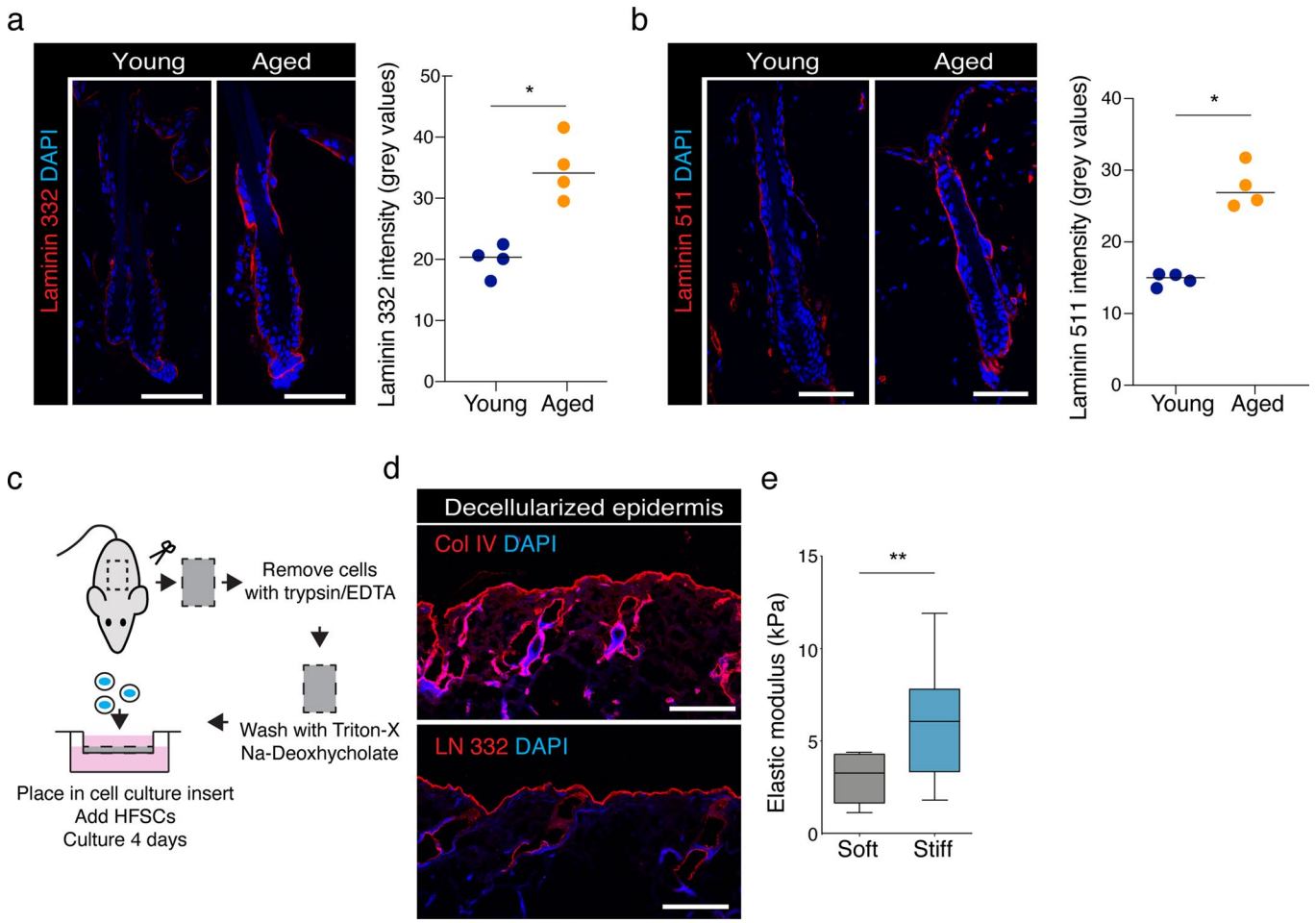

Extended Data Fig. 4 | Basement membranes in young and aged skin and decellularized scaffolds. a, Representative immunofluorescence images and quantification of Laminin 332 staining show increased levels in aged BMs (mean; n = 4 mice/group, *p = 0.0286, Mann-Whitney; Scale bars 50 µm). **b**, Representative immunofluorescence images and quantification of Laminin 511 staining show increased levels in aged BMs (mean; n = 4 mice/group, *p = 0.0286, Mann-Whitney; Scale bars 50 µm). **c**, Schematic illustration of decellularized basement membrane scaffold preparation from young and aged mice. **d**, Immunofluorescence images of decellularized basement membrane scaffolds showing absence of epidermal cell nuclei but intact basement membranes as marked by Collagen IV and Laminin 332 staining. A representative of 3 mice is shown. Scale bars 100 µm. **e**, Box and whiskers plot of atomic force microscopy force indentation measurements of 3 C organoid hydrogel stiffness (top, middle and bottom delimiters are the 75th, 50th, 25th percentiles; top and bottom whiskers are the maximum and minimum; n = 13 force curves pooled across 4 independent experiments; **p = 0.0012, Kolmogorov-Smirnov).

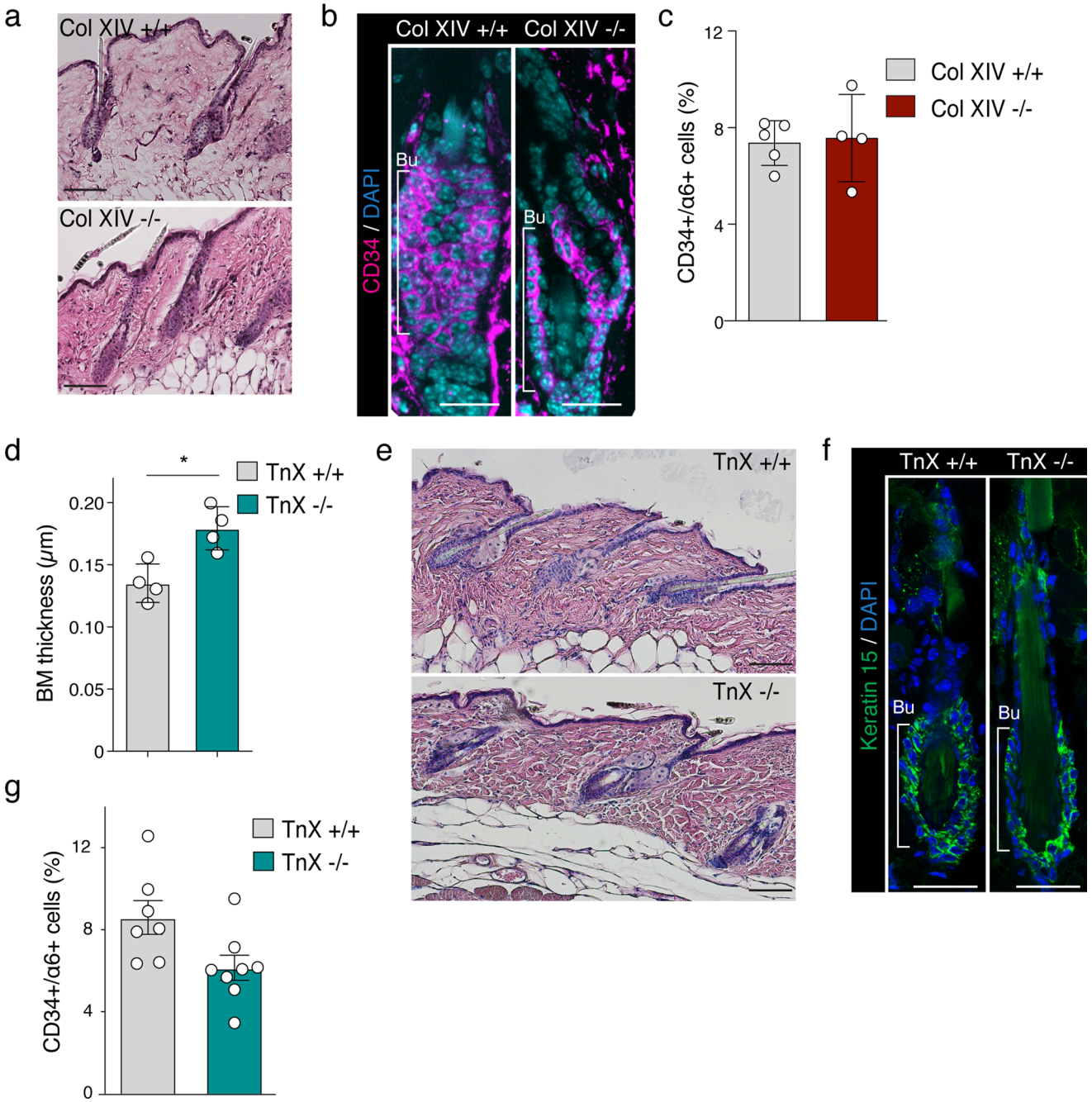

Extended Data Fig. 5 | Analyses of Collagen-XIV- and Tenascin-X-deficient mice. a, Hematoxylin/Eosin stainings from 1 year old Collagen-XIV-deficient (Col XIV -/-) and wild type (ColXIV +/+) control mice reveal no overt skin pathology. Scale bars 100 μm. Representative images from 3 mice/genotype are shown. **b**, Immunofluorescence images of Cd34 staining to mark the bulge (bu) niche from 1 year old Col XIV +/+ and -/- mice show comparable hair follicle morphology. Representative images from 3 mice/genotype are shown. Scale bars 25 μm. **c**, Quantification of CD34+/α6 integrin+ HFSCs by flow cytometry from 6 months old Col XIV +/+ and -/- mice shows no major reduction in levels of HFSCs (n = 5 Col XIV +/+ and n = 4 Col XIV -/- mice). **d**, Quantification of basement membrane (BM) thickness from skin electron micrographs of Tenascin-X-deficient (TnX -/-) and wild type (TnX +/+) control mice. Note increased BM thickness in TnX -/- mice (n = 4 mice/group; *p = 0.0286, Mann-Whitney). **e**, mHematoxylin/Eosin stainings from 1 year old TnX +/+ and TnX -/- mice show no overt skin pathology. Representative images from 3 mice/genotype are shown. Scale bars 100 μm. **f**, Immunofluorescence images of Keratin-15 staining to mark the bulge (bu) niche from 1 year old TnX +/+ and -/- mice show comparable hair follicle morphology. Representative images from 3 mice/genotype are shown. Scale bars 25 μm. **g**, Quantification of CD34+/α6 integrin+ HFSCs by flow cytometry from 6 months old TnX +/+ and -/- mice shows slightly reduced levels of HFSCs in TnX -/- mice (n = 7 TnX +/+ and n = 8 TnX -/- mice; *p = 0.0301, Student's t-test). Bar graphs show mean ±SD.

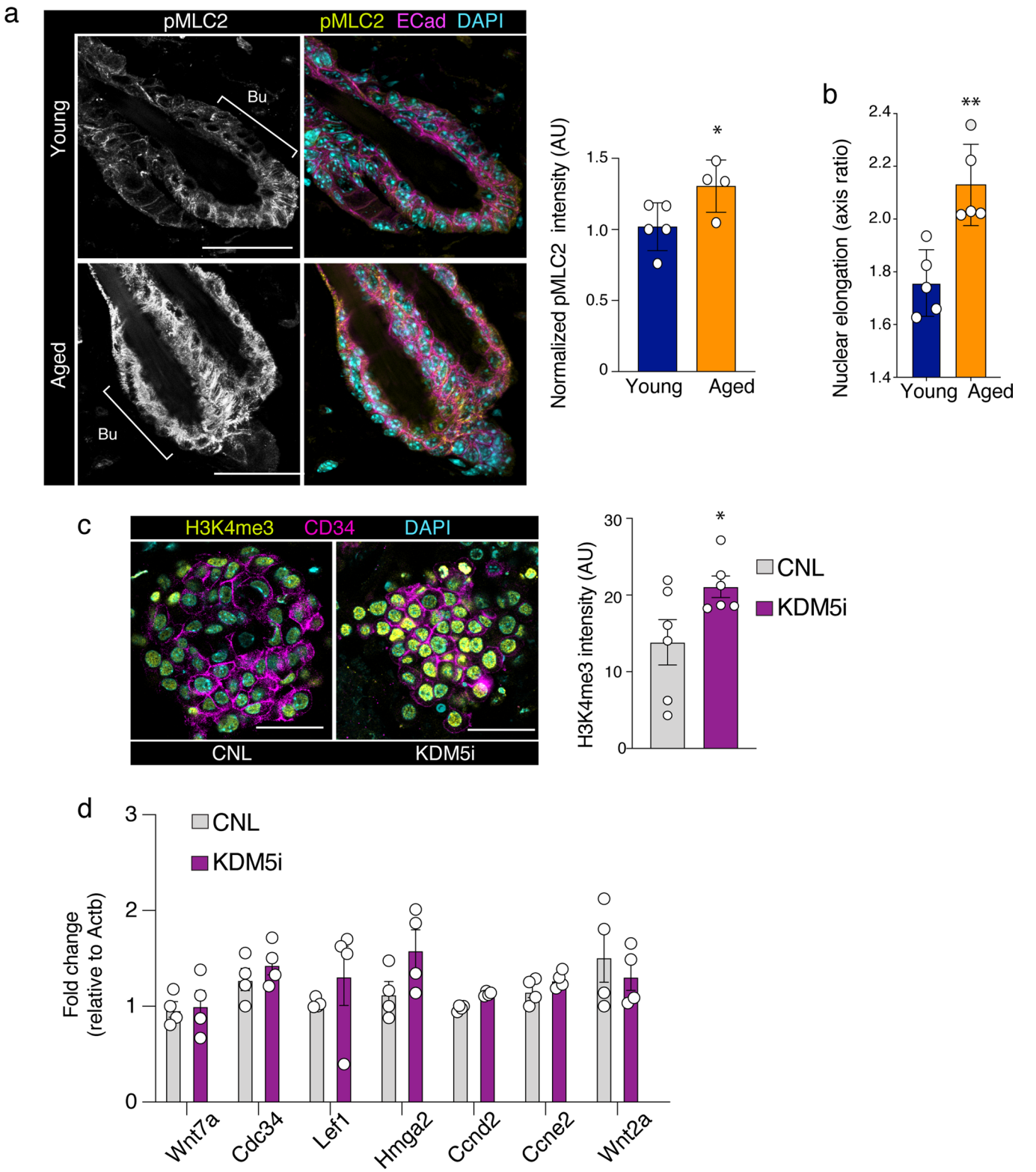

Extended Data Fig. 6 | Analyses of contractility and transcription in hair follicles and organoid cultures. a, Representative immunofluorescence images and quantification of phosphorylated myosin light chain 2 (pMLC2). Note increased pMLC2 indicating increased contractility in aged bulge (bu) HFSCs (n = 5 young and n = 4 aged mice; *p = 0.0451, Student's t-test; Scale bar 50 μm). **b**, Quantification of the nuclear aspect ratio (major axis/minor axis) shows increased nuclear elongation of aged HFSCs (n = 5 mice/group with >100 nuclei per mouse; **p = 0.0031, Student's t-test). **c**, Representative images and quantification of H3K4me3 intensity from HFSC organoids treated with Kdm5 inhibitor (Kdm5i) (n = 6 independent experiments; p = 0.0515, Student's t-test; Scale bar 50 μm). **d**, Quantitative RT-PCR of selected genes with bivalent promoter state from HFSC organoids treated with Kdm5i (n = 4 independent experiments). Bar graphs show mean ±SD.

nature research

Corresponding author(s): Sara A. Wickström

Last updated by author(s): May 25, 2021

Reporting Summary

Nature Research wishes to improve the reproducibility of the work that we publish. This form provides structure for consistency and transparency in reporting. For further information on Nature Research policies, see Authors & Referees and the Editorial Policy Checklist.

Statistics

For all statistical analyses, confirm that the following items are present in the figure legend, table legend, main text, or Methods section.

n/a	Confirmed
☐	☒ The exact sample size (*n*) for each experimental group/condition, given as a discrete number and unit of measurement
☐	☒ A statement on whether measurements were taken from distinct samples or whether the same sample was measured repeatedly
☐	☒ The statistical test(s) used AND whether they are one- or two-sided *Only common tests should be described solely by name; describe more complex techniques in the Methods section.*
☐	☒ A description of all covariates tested
☐	☒ A description of any assumptions or corrections, such as tests of normality and adjustment for multiple comparisons
☐	☒ A full description of the statistical parameters including central tendency (e.g. means) or other basic estimates (e.g. regression coefficient) AND variation (e.g. standard deviation) or associated estimates of uncertainty (e.g. confidence intervals)
☐	☒ For null hypothesis testing, the test statistic (e.g. *F*, *t*, *r*) with confidence intervals, effect sizes, degrees of freedom and *P* value noted *Give P values as exact values whenever suitable.*
☒	☐ For Bayesian analysis, information on the choice of priors and Markov chain Monte Carlo settings
☒	☐ For hierarchical and complex designs, identification of the appropriate level for tests and full reporting of outcomes
☒	☐ Estimates of effect sizes (e.g. Cohen's *d*, Pearson's *r*), indicating how they were calculated

Our web collection on statistics for biologists contains articles on many of the points above.

Software and code

Policy information about availability of computer code

Data collection	Leica Application Suite X (confocal microscopy, version 2.0.0.14332) Nikon NIS Elements D software (light microscopy, version 4.51) BD FACS Diva (Flow cytometry, version 8.0.1) JPK SPM Control Software (version 5) BioRad CFX384 Touch (PCR) Orbitrap Tribid (Mass spectrometry) Soft Imaging System GmbH analySIS (electron microscopy, version 3.1)
Data analysis	JPK Data Processing Software (Bruker Nano, version 5) GraphPad Prism software (GraphPad, version 8), Fiji (version 2.0.0) , FlowJo (BD Bioscience version 5.0) MaxQuant (version 1.5.2.8) R (version 3.5.2) Flexbar (version 2.5) BWA MEM (version 0.7.12) THOR (version 0.1) DeepTools (version 3.3.1) Integrative Genomics Viewer (version 2.4.14) Homer (version 4.10) Metascape ChIPseeker (version 1.2.6) STAR (version 2.5.2b) featureCounts (version 1.6.2) DEseq2 (version 1.22.2)

Macs2 (version 2.2.7.1)
DiffBind (version 2.14.0)
limma (version 3.34.9)

For manuscripts utilizing custom algorithms or software that are central to the research but not yet described in published literature, software must be made available to editors/reviewers. We strongly encourage code deposition in a community repository (e.g. GitHub). See the Nature Research guidelines for submitting code & software for further information.

Data

Policy information about availability of data

All manuscripts must include a data availability statement. This statement should provide the following information, where applicable:

- Accession codes, unique identifiers, or web links for publicly available datasets
- A list of figures that have associated raw data
- A description of any restrictions on data availability

Sequencing data that support the findings of this study have been deposited in the Gene Expression Omnibus (GEO) under accession code GSE148619. Proteomics data have been deposited to the ProteomeXchange Consortium via the PRIDE partner repository with the dataset identifier PXD018352. Previously published sequencing data that were re-analysed here are available under accession code GSE31239. All other data supporting the findings of this study are available from the corresponding author on reasonable request.
Data accession links:
https://www.ncbi.nlm.nih.gov/geo/query/acc.cgi?acc=GSE148619
http://proteomecentral.proteomexchange.org/cgi/GetDataset

Field-specific reporting

Please select the one below that is the best fit for your research. If you are not sure, read the appropriate sections before making your selection.

☒ Life sciences ☐ Behavioural & social sciences ☐ Ecological, evolutionary & environmental sciences

For a reference copy of the document with all sections, see nature.com/documents/nr-reporting-summary-flat.pdf

Life sciences study design

All studies must disclose on these points even when the disclosure is negative.

Sample size	Sample size was determined based on previous experience, published literature, or to specific requirements of a given technique. Sample size for each experiment is indicated in figure legends
Data exclusions	No data was excluded
Replication	All experiments were performed using at least three biological replicates, except ChIP sequencing, which were done in biological duplicates. Number of replicates for each experiment is indicated in the corresponding figure legend. Several steps were taken to ensure the reproducibility of experimental findings and key results were confirmed using complementary experimental approaches.
Randomization	Samples were not randomized, randomization was not relevant as samples were grouped according to age or genotype
Blinding	Blinding was not relevant as phenotypes of mice were clear to experimenters and automated software algorithms were used for unbiased quantification of staining intensities and sequencing data.

Reporting for specific materials, systems and methods

We require information from authors about some types of materials, experimental systems and methods used in many studies. Here, indicate whether each material, system or method listed is relevant to your study. If you are not sure if a list item applies to your research, read the appropriate section before selecting a response.

Materials & experimental systems

n/a	Involved in the study
☐	☒ Antibodies
☒	☐ Eukaryotic cell lines
☒	☐ Palaeontology
☐	☒ Animals and other organisms
☒	☐ Human research participants
☒	☐ Clinical data

Methods

n/a	Involved in the study
☐	☒ ChIP-seq
☐	☒ Flow cytometry
☒	☐ MRI-based neuroimaging

Antibodies

Antibodies used	CD34 (Thermo Fisher 14-0341-82, 1:100), Sox9 (Santa Cruz sc-20095, 1:100), Keratin-15 (Thermo Fisher MS-1068, 1:300), pMLC2 (Cell Signaling #3674, 1:100), RNA polymerase II phospho-S2 (Abcam ab5095, 1:900), Ki67 (Abcam ab15580, 1:1000), Lef1 (Cell Signaling #2230, 1:100), E-Cadherin (BD Biosciences 610181, 1:300), Laminin-332 (produced as described by Marinkovich,et al., J Biol Chem 1992; 1:20,000), Laminin alpha5 (produced as described in Sorokin et al. Exp Cell Res 2000; 1:20,000), CD34-eFluor 660 (Thermo Fisher Scientific 50-0341-82, 1:100) and ITGA6-eFluor 450 (Thermo Fisher Scientific 48-0495-82, 1:300), anti-BrdU (BD Biosciences 347580; 1:50), H3K27me3 (Cell Signaling #9733, 1:300) H3K4me3 (Cell Signaling #9727, 1:300), IgG control (Cell Signaling #5415), Collagen XIV (produced as described by Ansorge et al. J Biol Chem 2009).
Validation	All antibodies are well characterized and were applied according to datasheet instructions or previously published protocols. Antibodies were additionally validated as follows: For immunofluorescence: Antibodies were validated using knockout mouse models (Laminin 332, Laminin alpha5, Collagen XIV), or by observing expected pattern of histological staining and colocalization with additional markers of same state or process (CD34, Sox9, Keratin 15, pMLC2) or by the manufacturer (H3K4me3, RNA polymerase II phospho-S2). For ChIP: Antibodies were validated by the manufacturer (H3K27me3, H3K4me3, RNA polymerase II phospho-S2). For Flow cytometry: Antibodies were validated in non-expressing cells (CD34, ITGA6).

Animals and other organisms

Policy information about studies involving animals; ARRIVE guidelines recommended for reporting animal research

Laboratory animals	Wild-type C57Bl6J mice, Collagen XIV-deficient and Tenascin-X deficient mice at the age of 45-55 days, 6 or 24 months and CAnN.Cg-Foxn1nu/Crl BALB/c-nude mice at the age of 8 weeks were used. Nude mice were females, otherwise male mice were used.
Wild animals	Study did not involve wild animals
Field-collected samples	Study did not involve samples collected from the field
Ethics oversight	All animal experiments were approved by the local authorities (Ministry for Environment, Agriculture, Conservation and Consumer Protection of the State of North Rhine-Westphalia, Germany)

Note that full information on the approval of the study protocol must also be provided in the manuscript.

ChIP-seq

Data deposition

☒ Confirm that both raw and final processed data have been deposited in a public database such as GEO.

☒ Confirm that you have deposited or provided access to graph files (e.g. BED files) for the called peaks.

Data access links *May remain private before publication.*	https://www.ncbi.nlm.nih.gov/geo/query/acc.cgi?acc=GSE148619 http://proteomecentral.proteomexchange.org/cgi/GetDataset
Files in database submission	normalized_annotated_counts_all.results.tsv ATAC-seq.all_peaks.tsv H3K27me3.all_peaks.tsv H3K4me3.all_peaks.tsv Pol2.all_peaks.tsv Y68_R1.fastq.gz Y68_R2.fastq.gz Y69_R1.fastq.gz Y69_R2.fastq.gz Y70_R1.fastq.gz Y70_R2.fastq.gz O66_R1.fastq.gz O66_R2.fastq.gz O67_R1.fastq.gz O67_R2.fastq.gz O68_R1.fastq.gz O68_R2.fastq.gz K002000030_43546_y1_1.fq.gz K002000030_43546_y1_2.fq.gz K002000030_43547_y2_1.fq.gz K002000030_43547_y2_2.fq.gz K002000030_43548_y3_1.fq.gz K002000030_43548_y3_2.fq.gz K002000030_43549_y4_1.fq.gz K002000030_43549_y4_2.fq.gz K002000030_43550_o1_1.fq.gz

K002000030_43550_o1_2.fq.gz
K002000030_43551_o2_1.fq.gz
K002000030_43551_o2_2.fq.gz
K002000030_43552_o3_1.fq.gz
K002000030_43552_o3_2.fq.gz
K002000030_43553_o4_1.fq.gz
K002000030_43553_o4_2.fq.gz
Y1_128308_S2_R1.fastq.gz
Y1_128308_S2_R2.fastq.gz
Y2_128310_S4_R1.fastq.gz
Y2_128310_S4_R2.fastq.gz
Y3_128312_S6_R1.fastq.gz
Y3_128312_S6_R2.fastq.gz
O1_128314_S8_R1.fastq.gz
O1_128314_S8_R2.fastq.gz
O2_128316_S10_R1.fastq.gz
O2_128316_S10_R2.fastq.gz
O3_128318_S12_R1.fastq.gz
O3_128318_S12_R2.fastq.gz
K4_Y1_R1.fastq.gz
K4_Y1_R2.fastq.gz
K4_Y2_R1.fastq.gz
K4_Y2_R2.fastq.gz
K4_O1_R1.fastq.gz
K4_O1_R2.fastq.gz
K4_O2_R1.fastq.gz
K4_O2_R2.fastq.gz
Pol2_Y1_R1.fastq.gz
Pol2_Y1_R2.fastq.gz
Pol2_Y2_R1.fastq.gz
Pol2_Y2_R2.fastq.gz
Pol2_O1_R1.fastq.gz
Pol2_O1_R2.fastq.gz
Pol2_O2_R1.fastq.gz
Pol2_O2_R2.fastq.gz

Genome browser session
(e.g. UCSC)

no longer applicable

Methodology

Replicates

H3K27me3 ChIP seq experiment was performed with samples from 6 mice (3/ group), H3K4me3 and Pol2 ChIP seq experiments were both performed with 4 mice (2/ group)

Sequencing depth

H3K4me3: O1: 122477575 total reads, 121838992 mapped reads, 100bp read length, PE; O2: 114940366 total reads, 114389904 mapped reads, 100bp read length, PE; Y1: 106630359 total reads, 106189174 mapped reads, 100bp read length, PE; Y2: 118172143 total reads, 117550739 mapped reads, 100bp read length, PE
Pol2: O1: 100937625 total reads, 99943926 mapped reads, 100bp read length, PE; O2: 104591371 total reads, 103708980 mapped reads, 100bp read length, PE; Y1: 90627872 total reads, 89740454 mapped reads, 100bp read length, PE; Y2: 114699278 total reads, 113849265 mapped reads, 100bp read length, PE
H3K27me3: O1: 95684000 total reads, 95524812 mapped reads, 100bp read length, PE; O2: 93266602 total reads, 93089251 mapped reads, 100bp read length, PE; O3: 99893394 total reads, 99692490 mapped reads, 100bp read length, PE; Y1: 105790821 total reads, 105587257 mapped reads, 100bp read length, PE; Y2: 107570210 total reads, 107311055 mapped reads, 100bp read length, PE; Y3: 88565287 total reads, 88381140 mapped reads, 100bp read length, PE

Antibodies

H3K27me3: active motif, 39155, polyclonal
H3K4me3: Cell signaling, #9727, polyclonal
Pol2: Cell signaling ,#14958, clone D8L4Y

Peak calling parameters

Read mapping: BWA mem (version 0.7.12), standard parameters
Peak calling: macs2 (version 2.2.7.1), Pol2 and H3K4me3: standard parameters, PE mode, H3K27me3: broad peaks, PE

Data quality

Sequencing quality was checked using FastQC (version 0.11.9), Mapping quality was checked using Picard (version 2.23.9), variability between experimental conditions was checked using PCA plot from DiffBind (version 2.14.0), coverage profiles were visualized using IGV browser (version 2.4.14).
H3K4me3: FDR 5% and above 5-fold enrichment: O1: 7451, O2: 9920, Y1: 15855, Y2: 12253
Pol2: FDR 5% and above 4-fold enrichment: O1: 1289, O2: 2431, Y1: 5893, Y2: 20308
H3K27me3: FDR 5% and above 3-fold enrichment: O1: 12935, O2: 6019, O3: 8555, Y1: 4830, Y2: 9384, Y3: 12616

Software

FastQC (version 0.11.9) was used to check Sequencing quality, Trimmomatic (version 0.32) was used to trim adapters, reads were aligned using BWA mem (version 0.7.12), peak calling was done using macs2 (version 2.2.7.1), differential binding was detected using DiffBind (version 2.14.0), heatmaps and clustering was done using deeptools (version 3.3.1).

Flow Cytometry

Plots

Confirm that:

☒ The axis labels state the marker and fluorochrome used (e.g. CD4-FITC).

☒ The axis scales are clearly visible. Include numbers along axes only for bottom left plot of group (a 'group' is an analysis of identical markers).

☒ All plots are contour plots with outliers or pseudocolor plots.

☒ A numerical value for number of cells or percentage (with statistics) is provided.

Methodology

Sample preparation	For freshly isolated epidermal cells, single cell suspensions were generated by incubating skin pieces in 0.8% trypsin for 50 min. For 3C organoids, Matrigel droplets were degraded for 8 min at 37°C using 0.5% Trypsin, 0.5 mM EDTA in PBS. Trypsin was neutralized using FACS buffer (2 mM EDTA, 2% FBS in PBS). Cells were then pelleted by centrifugation for 5 min at 2000 rpm at 4°C, resuspended in FACS buffer and stained for cell surface markers CD34-eFluor 660 (Thermo Fisher Scientific 50-0341-82, 1:100) and ITGA6-eFluor 450 (Thermo Fisher Scientific 48-0495-82, 1:300), on ice. 7AAD (Thermo) for detection of live/dead cells was added to each sample 15 min before the analysis.
Instrument	Cells were analyzed using FACSCanto II (BD Biosciences) or sorted using FACSAria IIIu Svea (BD Biosciences) and/or FACSAria Fusion (BD Biosciences).
Software	Flow cytometry data was collected with BD FACS Diva software (version 8.0.1) and analyzed with FlowJo (version 5.0).
Cell population abundance	Purity was confirmed with a post-sort purity FACS (95-98). The relevant cell population (HFSCs) represented 5-12% of the total live cell population and was between 100-250K cells per mouse.
Gating strategy	The following gating strategy was used: 1. Forward scatter (FSC) area vs. side scatter (SSC) area plot with gate 1 to separate cell events from debris. 2. FSC width vs FSC area plot with gate 2 to separate single cells from doublets. 3. SSC width vs SSC area plot with gate 3 to further separate single cells from doublets. 4. 7AAD vs FSC area plot with gate 4 to separated live from dead cells. 5. ITGA6-eFluor 450 vs CD34-eFluor 660 plot with quad gate shows in 2nd quadrant ITGA6+ CD34+ HFSCs. Gates were set according to single stain control. A figure exemplifying the strategy is provided in Supplementary Figure 1.

☒ Tick this box to confirm that a figure exemplifying the gating strategy is provided in the Supplementary Information.